

## Weather Forecasts by the WRF-ARW Model with the GSI Data Assimilation System in the Complex Terrain Areas of Southwest Asia

J. XU

*University Corporation for Atmospheric Research, Boulder, Colorado, and Air Force Weather Agency, Offutt Air Force Base, Nebraska, and Joint Center for Satellite Data Assimilation, Camp Springs, Maryland*

S. RUGG AND L. BYERLE

*Air Force Weather Agency, Offutt Air Force Base, Nebraska*

Z. LIU

*National Center for Atmospheric Research, Boulder, Colorado*

(Manuscript received 10 November 2008, in final form 5 January 2009)

### ABSTRACT

This paper will first describe the forecasting errors encountered from running the National Center for Atmospheric Research (NCAR) mesoscale model (the Advanced Research Weather Research and Forecasting model; ARW) in the complex terrain of southwest Asia from 1 to 31 May 2006. The subsequent statistical evaluation is designed to assess the model's surface and upper-air forecast accuracy. Results show that the model biases caused by inadequate parameterization of physical processes are relatively small, except for the 2-m temperature, as compared to the nonsystematic errors resulting in part from the uncertainty in the initial conditions. The total model forecast errors at the surface show a substantial spatial heterogeneity; the errors are relatively larger in higher mountain areas. The performance of 2-m temperature forecasts is different from the other surface variables' forecasts; the model forecast errors in 2-m temperature forecasts are closely related to the terrain configuration. The diurnal cycle variation of these near-surface temperature forecasts from the model is much smaller than what is observed.

Second, in order to understand the role of the initial conditions in relation to the accuracy of the model forecasts, this study assimilated a form of satellite radiance data into this model through the Joint Center for Satellite Data Assimilation (JCSDA) analysis system called the Gridpoint Statistical Interpolation (GSI). The results indicate that on average over a 30-day experiment for the 24- and 48-h (second 24 h) forecasts, the satellite data provide beneficial information for improving the initial conditions and the model errors are reduced to some degree over some of the study locations. The diurnal cycle for some forecasting variables can be improved after satellite data assimilation; however, the improvement is very limited.

### 1. Introduction

Weather prediction in southwest Asia (SWA) is often very complex because of mesoscale variations induced by the diverse topography. This is predominately a semi-arid to arid region surrounded by the Black and Caspian Seas to the north, the Mediterranean to the west, the Arabian Sea and Persian Gulf to the south, the Hima-

layas to the east, and crossed by the impressive Tauros, Zagros, and Hindu Kush mountains. A few previous model studies (Evans and Smith 2001, 2006; Evans et al. 2004; Zaitchik et al. 2007a,b; Marcella and Eltahir 2008) provided some interesting results for the basic weather simulation in SWA using a regional climate model [the second-generation National Center for Atmospheric Research (NCAR) Regional Climate Model (RegCM2)] or the fifth-generation Pennsylvania State University-NCAR Mesoscale Model (MM5) model. They pointed out that the regional model has difficulty producing an accurate simulation of precipitation in certain subregions, which is related to an accurate description of

---

*Corresponding author address:* Dr. Jianjun Xu, Joint Center for Satellite Data Assimilation, WWB, 5200 Auth Rd., Camp Springs, MD 20746.  
E-mail: jianjun.xu@noaa.gov

storm tracks, topographic interactions, and atmospheric stability. However, for a next-generation mesoscale forecast model (the Advanced Research Weather Research and Forecasting model, ARW) developed by NCAR (Skamarock et al. 2005), the performance of this model employed in the operational forecasts over this region is not fully understood. One of the purposes in this paper is to evaluate the performance of the ARW model in SWA complex terrain.

This evaluation primarily concentrates on the forecasts of wind, temperature, and precipitation since SWA is dominated by hot, dusty, windy weather (Agrawala et al. 2001). During the transitional season from winter to summer, the temperature and wind increase substantially; contrastingly, the precipitation decreases significantly. Subsequently, during this seasonal transition, the occurrence of blowing sand/dust and unstable local-scale weather events increases as well, and the prediction accuracy of these events is highly dependent upon the accuracy of the temperature, precipitation, and wind forecasts from the model.

Some recent studies have evaluated the ARW model based on objective error statistics for precipitation forecasts over the United States. Cheng and Steenburgh (2005) produced surface sensible weather forecasts with ARW and Eta models over the western United States. Their results suggest that improvements in initialization may be as important, or more so, than improvements in the physics for land surface processes. Gallus and Bresch (2006) compared the impacts of Weather Research and Forecasting (WRF) model dynamics core, physics package, and initial conditions on warm season rainfall forecasts over the central United States. They found that the sensitivity of rainfall forecasts is a function of model physics, dynamics, and initial conditions, and they are situationally dependent on which dominates most. For heavier rainfall, sensitivity to initial conditions is generally less substantial than the sensitivity to changes in the dynamic core or physics. For light rainfall, the WRF model using NCAR physics is much more sensitive to a change in the dynamic core than the WRF model using the National Centers for Environmental Prediction (NCEP) physics. It is very clear that the errors in the weather forecasts are caused by many reasons. One of these reasons is attributed to the imperfection of the numerical weather models' representation of the actual atmosphere. However, as Lorenz (1963) pointed out, the most fundamental cause of forecast failure is that the atmosphere is sensitive to initial conditions (ICs). This means that an arbitrarily small error in the analysis of the initial state of the atmosphere can have an overwhelming effect in a finite amount of time. Therefore, it is not surprising that

considerable effort has focused on improving the estimates of the model initial states through advanced techniques. One such technique is data assimilation. Thus, the second purpose of this paper is to evaluate the impact of data assimilation on weather forecasts over SWA areas.

This paper is organized as follows. Section 2 describes the real-time configuration of WRF-ARW as run operationally within SWA. The observational datasets used in the verification are given in section 3. Section 4 explains the methodology used in the evaluation. The results of the forecast error for the May 2006 case are presented in section 5. Section 6 investigates the impact of data assimilation on the forecasts. Finally, a summary and discussion are given in section 7.

## 2. WRF-ARW model and forecasts

The weather model used in this study is the WRF model utilizing the Advanced Research WRF dynamical core (WRF-ARW; Michalakes et al. 2001; Skamarock et al. 2005), which is a nonhydrostatic, fully compressible, primitive equation model. Lead institutions involved in the effort include NCAR, the Air Force Weather Agency (AFWA), the National Oceanic and Atmospheric Administration (NOAA), and other governmental agencies as well as several universities. WRF is built around a software architectural framework within which different dynamical cores and model physics packages are accessible within the same code. Within the WRF framework, it is possible to mix the dynamical cores with differing physics packages to optimize performance since each core has strengths and weaknesses in different areas. WRF-ARW uses a terrain-following pressure coordinate and the Arakawa C grid staggering.

Similar to AFWA operational setups, a 15-km grid spacing centered over SWA (Fig. 1) is used to encompass the region's complex topography and its associated spatial variability in surface characteristics. To assess model predictive skill, 48-h forecasts are made for each day starting at 0000 UTC for the period 1–31 May 2006. Forecasts without data assimilation are labeled CTRL in order to distinguish them from the forecasts with data assimilation found in section 6. The initial atmospheric and lateral boundary conditions, including soil moisture and temperature, are taken from the NCEP Global Forecast System (GFS) real-time forecasts at 3-h intervals, which are gridded to a horizontal resolution of  $1^\circ \times 1^\circ$ . Through the WRF Preprocessing System (WPS), the global soil categories, land-use category, terrain height, annual mean deep soil temperature, monthly

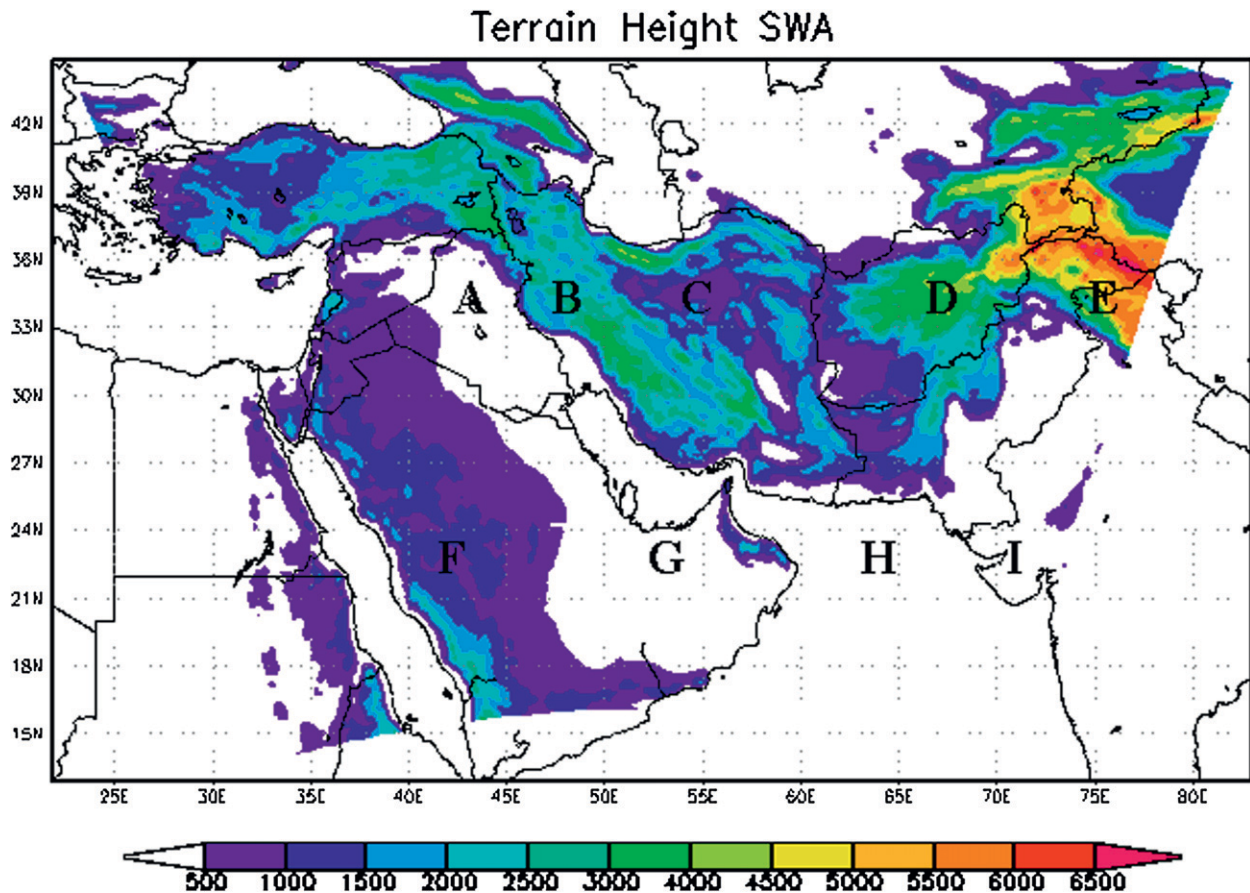


FIG. 1. Domain of the model and subregion definitions. Shading indicates the elevation of terrain (m). The subregions are defined as northern Iraq (A; 34°–36°N, 41°–43°E), northwestern Iran (B; 34°–36°N, 46°–48°E), north-central Iran (C; 34°–36°N, 54°–56°E), central Afghanistan (D; 34°–36°N, 66°–68°E), the western Himalayan Mountains (E; 34°–36°N, 74°–76°E), western Saudi Arabia (F; 22°–24°N, 41°–43°E), eastern Saudi Arabia (G; 22°–24°N, 51°–53°E), the Arabian Sea (H; 22°–24°N, 63°–65°E), and northwestern India (I; 22°–24°N, 70°–72°E).

vegetation fraction, monthly albedo, maximum snow albedo, and slope category are interpolated into the model grids of the study domain. The physics packages chosen are the WRF single-moment five-class (WSM5) microphysics scheme, the Yonsei University planetary boundary layer (YSUPBL) scheme, the Noah land surface scheme, the Grell–Devenyi ensemble cumulus scheme, the Rapid Radiative Transfer Model (RRTM) longwave radiation, and the Dudhia shortwave radiation scheme.

### 3. Observed and analyzed datasets

#### a. Observed precipitation

The observed precipitation data are taken from the Climate Prediction Center's (CPC) Famine Early Warning System (FEWS) program, which is derived from geostationary satellite retrieval precipitation data merged

with rain gauge data and model analysis. The merging technique has been shown to significantly reduce bias and random error compared to individual precipitation data sources, thus increasing the accuracy of the rainfall estimates (Xie and Arkin 1996a). Geostationary satellite data are utilized for the determination of cloud-top temperature. *Meteosat-5* thermal infrared (IR) digital data at 5-km-pixel resolution are accessed every 30 min and then reformatted and converted to a geographic grid with 0.1° resolution. The grid is 751 × 501 points, which begins with point (1, 1) at 10°N, 20°E and ends at point (751, 501) at 60°N, 95°E. A horizontal resolution of 0.1° was chosen for the estimate computations to correspond with the absolute positioning error for the satellite of approximately 10 km. Arrays are used to accumulate the occurrences of cloud-top temperatures below temperatures of 235 and 275 K. Rain gauge reports transmitted via the Global Telecommunications System (GTS) are received every 6 h and are utilized in

TABLE 1. The average height (m) of topography, vegetation type (Veg), and soil type (Soil) in the nine subregions (defined in Fig. 1) over SWA.

|        | A      | B     | C         | D          | E             | F          | G      | H     | I                      |
|--------|--------|-------|-----------|------------|---------------|------------|--------|-------|------------------------|
| Height | 328    | 2557  | 737       | 3833       | 4839          | 958        | 67     | 0     | 75                     |
| Veg    | Barren | Grass | Barren    | Shrub land | Wooded tundra | Barren     | Barren | Water | Mixed dryland/cropland |
| Soil   | Loam   | Loam  | Clay loam | Loam       | Loam          | Sandy loam | Loam   | Water | Loam                   |

the CPC Climate Assessment Data Base (CADB) for monitoring of climate anomalies. Automated quality control of these GTS observations within the CADB is done prior to the processing of precipitation estimates.

### b. Observed temperature

The maximum and minimum temperatures at 2-m levels with  $0.5^\circ \times 0.5^\circ$  gridded datasets are created by the CPC, which is taken from observational stations of the World Meteorological Organization (WMO) GTS datasets. The interpolation method is based on the previous rainfall estimation algorithm (Xie et al. 1996b).

### c. Analyzed temperature and wind field

The temperature and wind fields are taken from the NCEP GFS analysis data, which is gridded to a horizontal resolution of  $1^\circ \times 1^\circ$ .

## 4. Topography and evaluation method

To investigate the spatial heterogeneity of the complex terrain in SWA, nine representative subregions are depicted in Fig. 1. They are defined as northern Iraq (A;  $34^\circ\text{--}36^\circ\text{N}$ ,  $41^\circ\text{--}43^\circ\text{E}$ ), northwestern Iran (B;  $34^\circ\text{--}36^\circ\text{N}$ ,  $46^\circ\text{--}48^\circ\text{E}$ ), north-central Iran (C;  $34^\circ\text{--}36^\circ\text{N}$ ,  $54^\circ\text{--}56^\circ\text{E}$ ); central Afghanistan (D;  $34^\circ\text{--}36^\circ\text{N}$ ,  $66^\circ\text{--}68^\circ\text{E}$ ), west Himalayan Mountains (E;  $34^\circ\text{--}36^\circ\text{N}$ ,  $74^\circ\text{--}76^\circ\text{E}$ ), western Saudi Arabia (F;  $22^\circ\text{--}24^\circ\text{N}$ ,  $41^\circ\text{--}43^\circ\text{E}$ ), eastern Saudi Arabia (G;  $22^\circ\text{--}24^\circ\text{N}$ ,  $51^\circ\text{--}53^\circ\text{E}$ ), the Arabian Sea (H;  $22^\circ\text{--}24^\circ\text{N}$ ,  $63^\circ\text{--}65^\circ\text{E}$ ), and western India (I;  $22^\circ\text{--}24^\circ\text{N}$ ,  $70^\circ\text{--}72^\circ\text{E}$ ).

The nine subregions effectively represent the heterogeneity of the complex terrain in SWA. Table 1 displays the average topography (Hgt), vegetation type (Veg), and soil type (Soil) over these nine regions. Except for the water type in the Arabian Sea (marked H), the soil types in all other eight regions are loam; in addition, the vegetation types include barren, grass, shrubland, wooded land, mixed dry/cropland, and water. Three regions (B, D, and E) with terrain above 2500 m are covered by short plants with grass (B), shrubland (D), and wooded tundra (E). Three regions with terrain under 1000 m (A, C, and F) and the two plains regions (G and I) are practically free of any plants.

This evaluation is designed to present the model errors of surface temperatures, precipitation, wind speeds, and upper-atmospheric variables for both 24- and 48-h (e.g., the second 24 h) forecasts. The statistical measures used to quantify model forecast performance are bias (forecast – observation), mean-square error (MSE), and error standard deviation (SD). For purposes of interpretation, the MSE represents the total model forecast error including contributions from both systematic and nonsystematic/random errors. Systematic error may be caused by a consistent misrepresentation of physical parameters such as radiation or model convection. Nonsystematic errors are caused by uncertainties in the model initial conditions or unresolvable differences in the scales between the forecasts and observations (Nutter and Manobianco 1999).

If  $X$  represents any of the parameters under consideration for a given time and vertical level, then forecast error is defined as  $X' = X_f - X_a$ , where the subscripts  $f$  and  $a$  denote forecast and analyzed/observed quantities, respectively. Given  $N$  valid pairs of forecasts and analyses, the bias is computed as

$$\text{bias} = \overline{X'} = \frac{1}{N} \sum_{i=1}^N X'_i; \quad (1)$$

the mean-square error is computed as

$$\text{MSE} = \frac{1}{N} \sum_{i=1}^N (X'_i)^2; \quad \text{and} \quad (2)$$

the SD error is computed as

$$\text{SD} = \left[ \frac{1}{N} \sum_{i=1}^N (X'_i - \overline{X'})^2 \right]^{1/2}. \quad (3)$$

In Eqs. (1)–(3),  $N$  is used rather than  $N-1$  so that a decomposition following Murphy [(1988), Eq. (9)] could be applied to the MSE:

$$\text{MSE} = (\overline{X'})^2 + (\text{SD})^2. \quad (4)$$

Therefore, the total model forecast error (e.g., MSE) consists of contributions from model squared biases

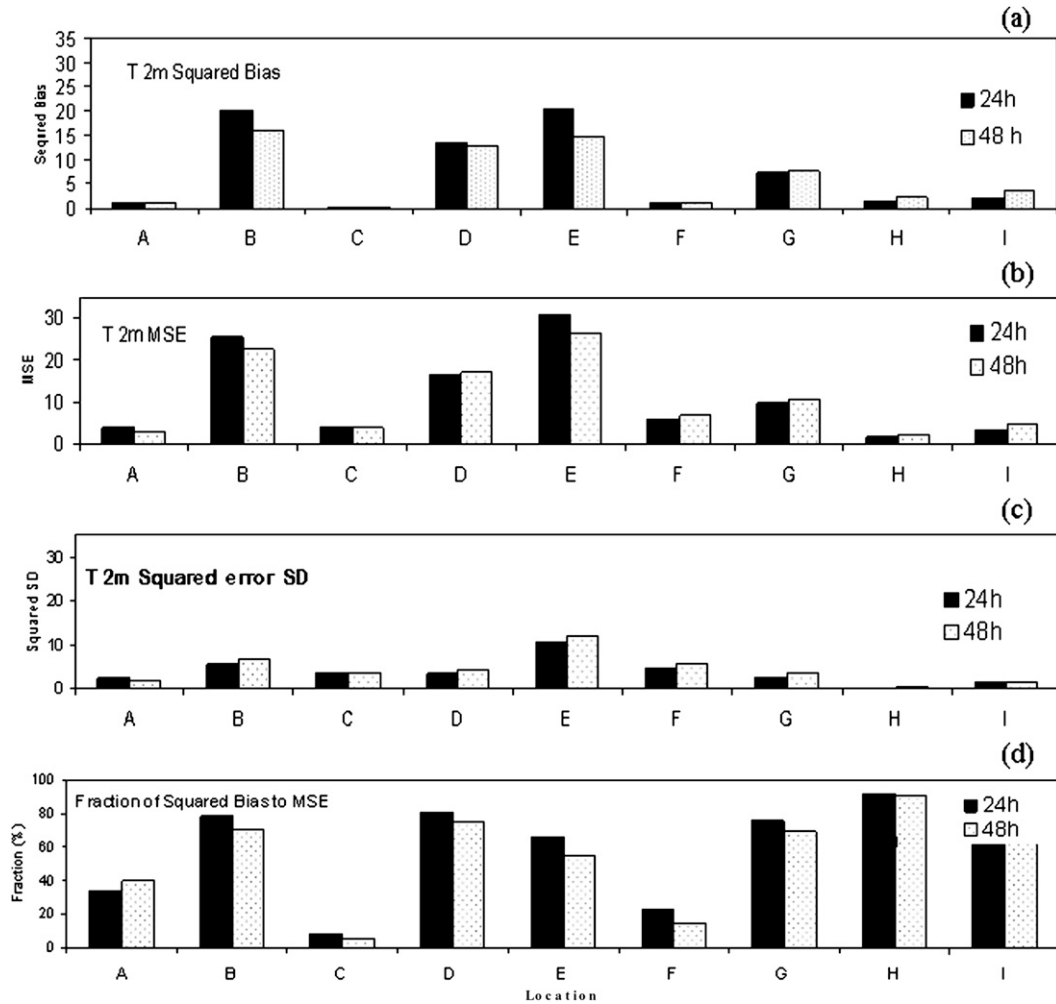


FIG. 2. Squared bias, MSE, squared SD error, and fraction of squared bias to MSE ( $E_r$ ) for 2-m temperature ( $T_{2m}$ , °C) forecasts from 1 to 31 May 2006. Results are plotted for averaged 24- and 48-h forecasts as a function of the locations (A, B, C, D, E, F, G, H, and I) defined in Fig. 1. Unit is  $(^{\circ}\text{C})^2$  in (a),(b), and (c).

$(\overline{X'})^2$  (i.e., systematic error) and the squared standard deviation (SD)<sup>2</sup> error (i.e., nonsystematic error) in the forecast and observed data. A fraction is defined to indicate the ratio of systematic error in the total model forecast error as follows:

$$E_r = [(\overline{X'})^2/\text{MSE}]100\%. \quad (5)$$

Note in Eq. (5) that if the model bias is less than 50%, most of the MSE is due to random, nonsystematic-type variability in the errors.

### 5. Forecasts error

In the following section, WRF-ARW model forecast error characteristics for 24- and 48-h (e.g., second 24 h) forecasts and the diurnal variation are described. Re-

sults are from forecasts made during the 30-day period starting 1 through 30 May 2006.

#### a. 24- and 48-h forecasts

##### 1) TEMPERATURE AT 2 M

Squared biases (WRF forecasts – GFS analysis) in 2-m temperature forecasts vary with terrain elevation (Fig. 2a). Biases are larger over high-terrain areas (E, B, and D) for the 24- and 48-h forecasts. Meanwhile, the biases are significantly smaller in low-terrain regions (A, C, F, G, and I) or water areas (H).

Even though the magnitude of the squared error SD (Fig. 2c) in the highest-terrain region (E: western Himalayan Mountains) is nearly equivalent to that of the forecast bias, it is very small in the other areas. However, the biases and corresponding MSEs are comparable in

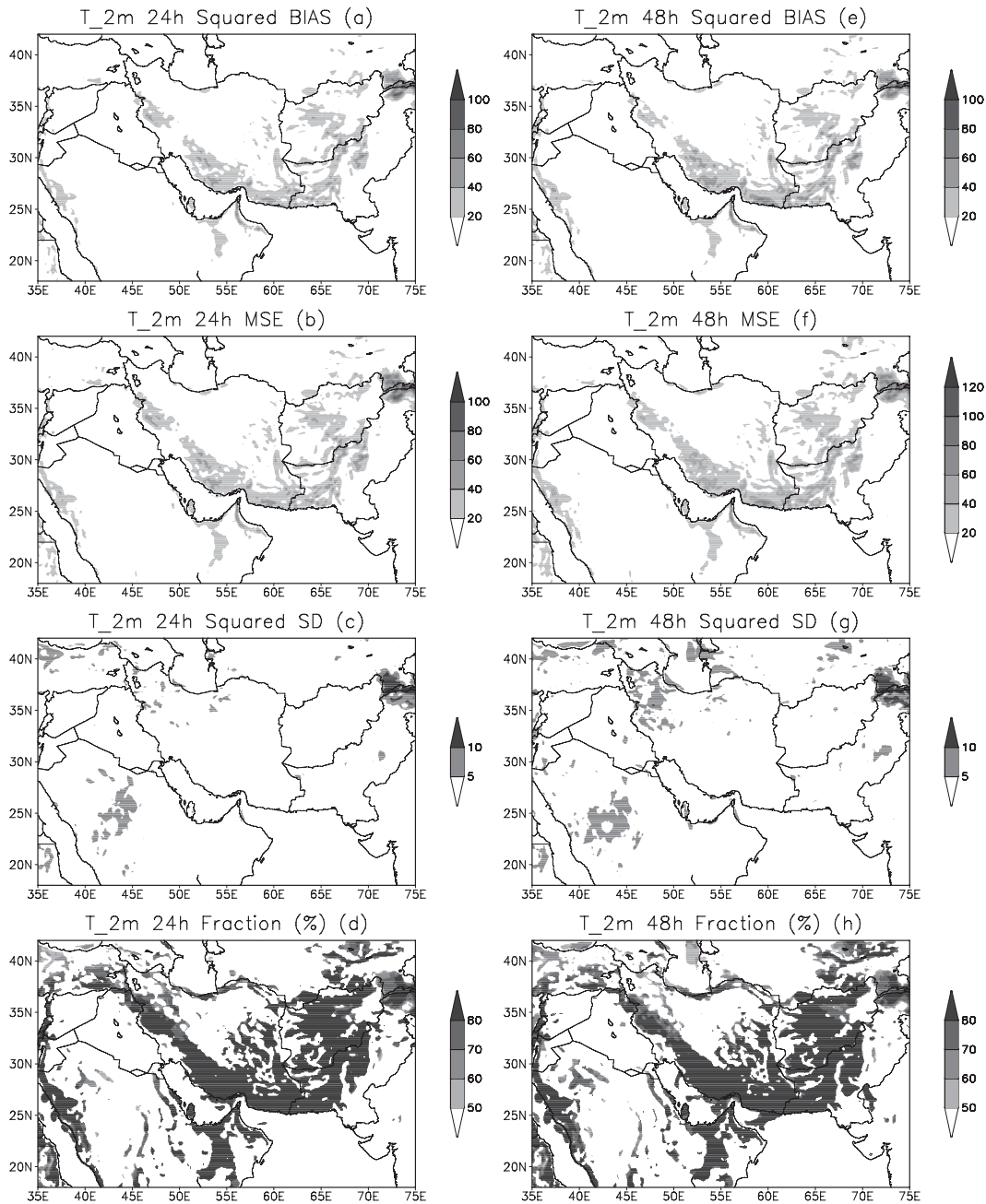


FIG. 3. Squared bias, MSE, squared SD error, and fraction of squared bias to MSE ( $E_r$ ) of  $T_{2m}$  for (a)–(d) 24- and (e)–(h) 48-h forecasts for 30-day averages from 1 to 31 May 2006. Unit is  $(^{\circ}\text{C})^2$  in (a)–(c) and (e)–(g).

magnitude over most of other mountainous areas (Fig. 2b). The fraction of the squared biases to the MSEs (Fig. 2d) is greater than 50% in most of the areas, which showed clearly that a large contribution to the total model forecasts error in these locations is derived from a systematic model error. The results indicate an apparent model deficit in the description of surface temperature in high-terrain areas.

To illustrate the above point, squared biases, MSEs, and squared SD errors in the whole of SWA are depicted in Fig. 3. For the 24-h forecasts, the total model forecast errors are dominated by the model systematic errors (Figs. 3a–c). The fraction of squared biases to the MSEs (Fig. 3d) exceeds 50%; the distribution of the total model forecast errors is also dependent on the configuration of the terrain (cf. Figs. 3a,b and Fig. 1).

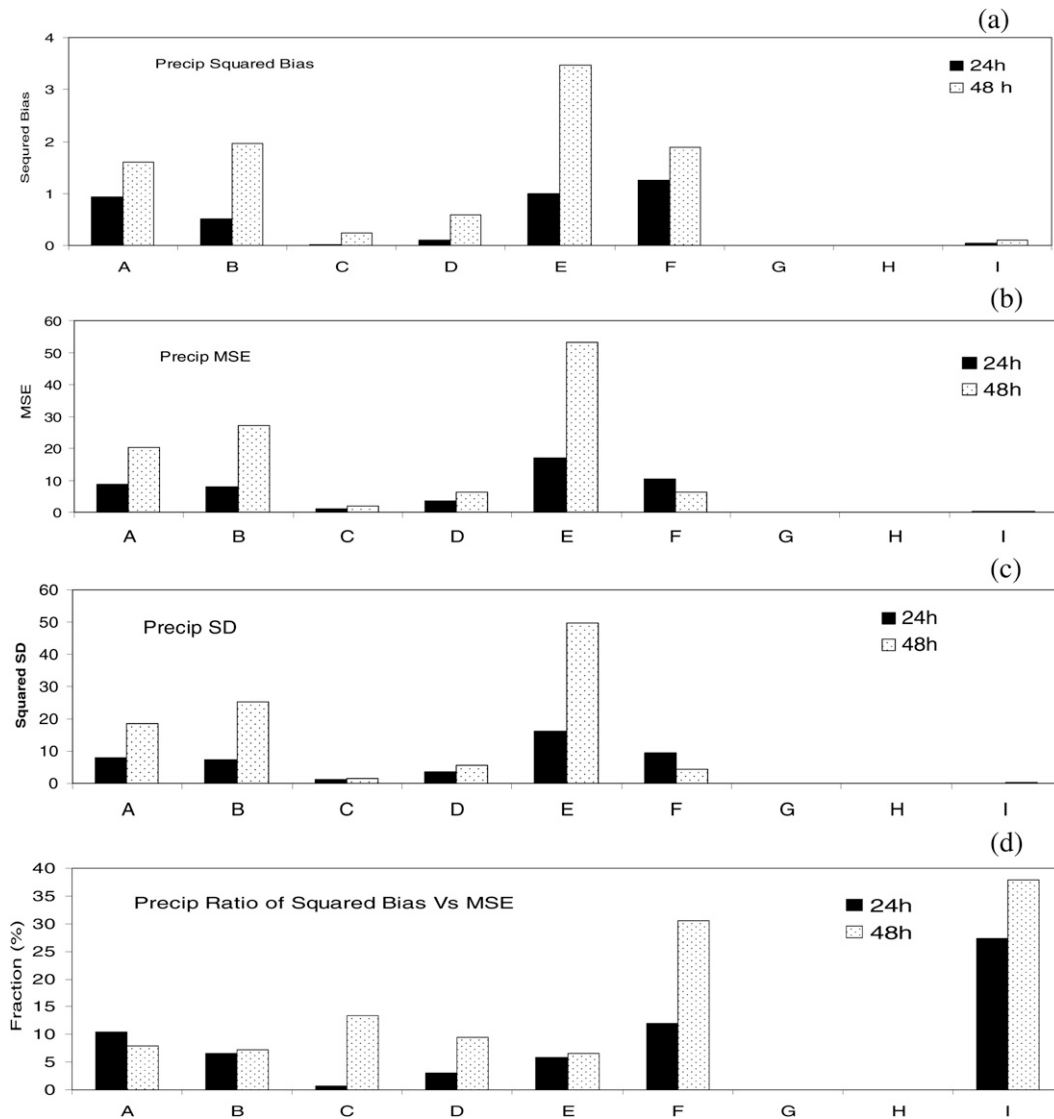


FIG. 4. Same as in Fig. 2 but for precipitation ( $\text{mm day}^{-1}$ ) forecasts. Units are  $(\text{mm day}^{-1})^2$  in (a)–(c).

The 48-h forecast errors are a little higher than the 24-h forecast errors (Figs. 3e–h).

## 2) PRECIPITATION

In contrast, the precipitation MSEs in the 24-h forecasts are dominated by the squared SD error (Fig. 4) over all nine selected subregions. The biases are not correlated to the height of the terrain. The maximum of the squared bias (Fig. 4a) over the highest-terrain region is much smaller than the squared SD error. The fraction of the squared biases to the MSEs (Fig. 4d) is far less than 50% in all selected subregions, which showed clearly that a larger contribution to the total

model forecasts error comes from a nonsystematic model error. These results indicate an apparent model problem in the description of the initial conditions or the model resolution. The 48-h forecast errors are much higher than the 24-h forecast errors in most areas.

For the whole study domain, the MSEs in the 24-h forecasts are obviously dominated by the model nonsystematic errors (Figs. 5a–c). The fraction of squared biases to the MSEs (Fig. 5d) is under 50% except for some Himalayan Mountains areas. The distribution of the total model forecast errors has nothing to do with the structure of the higher terrain. The areas of the 48-h forecast errors greater than  $20 \text{ mm}^2$  clearly expanded (Figs. 5e–h).

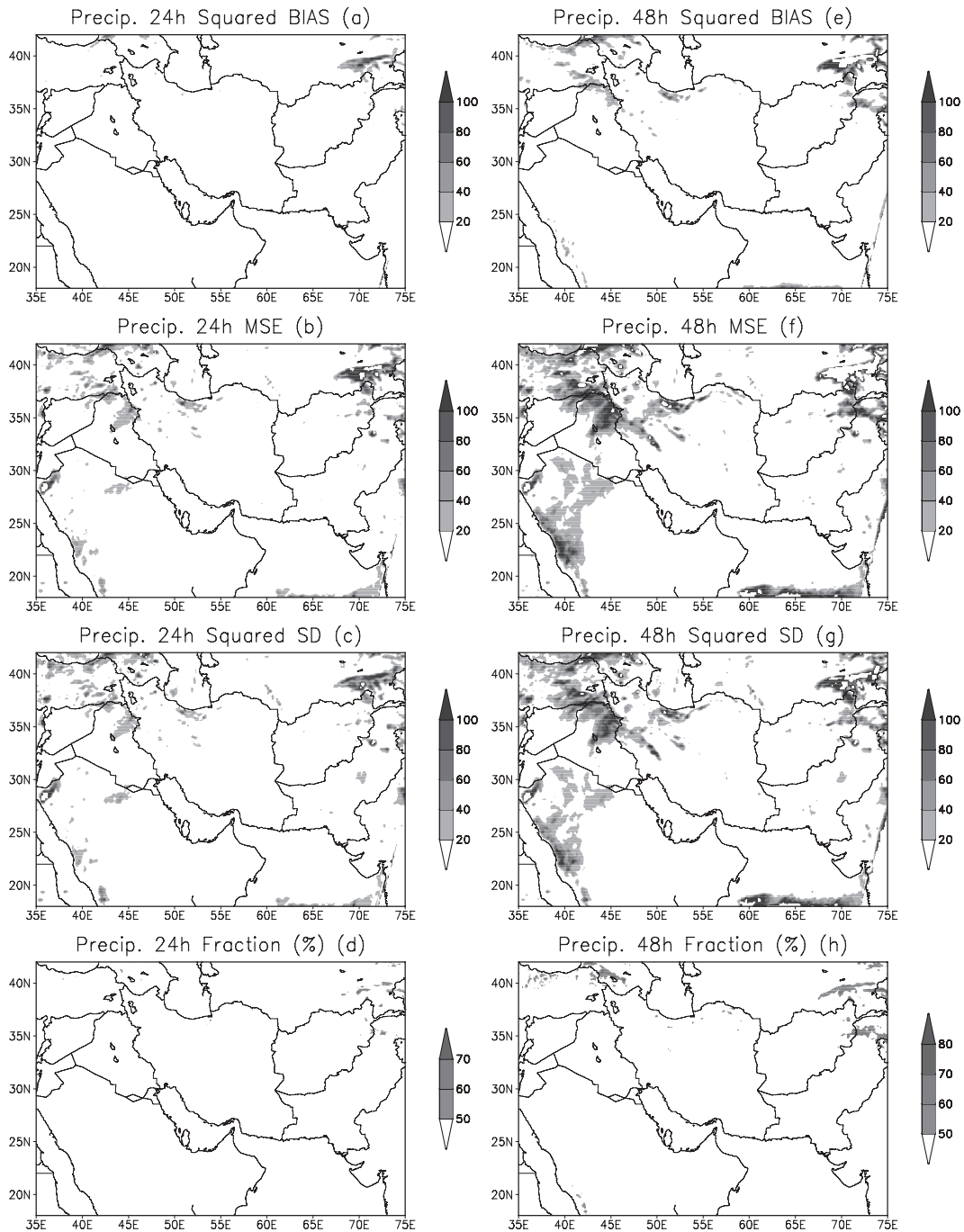


FIG. 5. Same as in Fig. 3 but for precipitation ( $\text{mm day}^{-1}$ ) forecasts. Units are  $(\text{mm day}^{-1})^2$  in (a)–(c) and (e)–(g).

### 3) WIND SPEED AT 10 M

Similar to precipitation, the MSEs in 10-m wind speed are largely associated with the nonsystematic errors in most of the subregions (Figs. 6a–c). The largest model bias occurs over northwestern Iran (Fig. 6a). The biases

over the western Himalayan Mountains region, eastern Saudi Arabia, and western India are almost zero. The fractions of the squared biases to the MSEs (Fig. 5d) are under 50% over all of the selected areas.

Over the SWA domain, the MSEs of the 10-m wind speed in the 24-h forecasts correspond fairly well to the

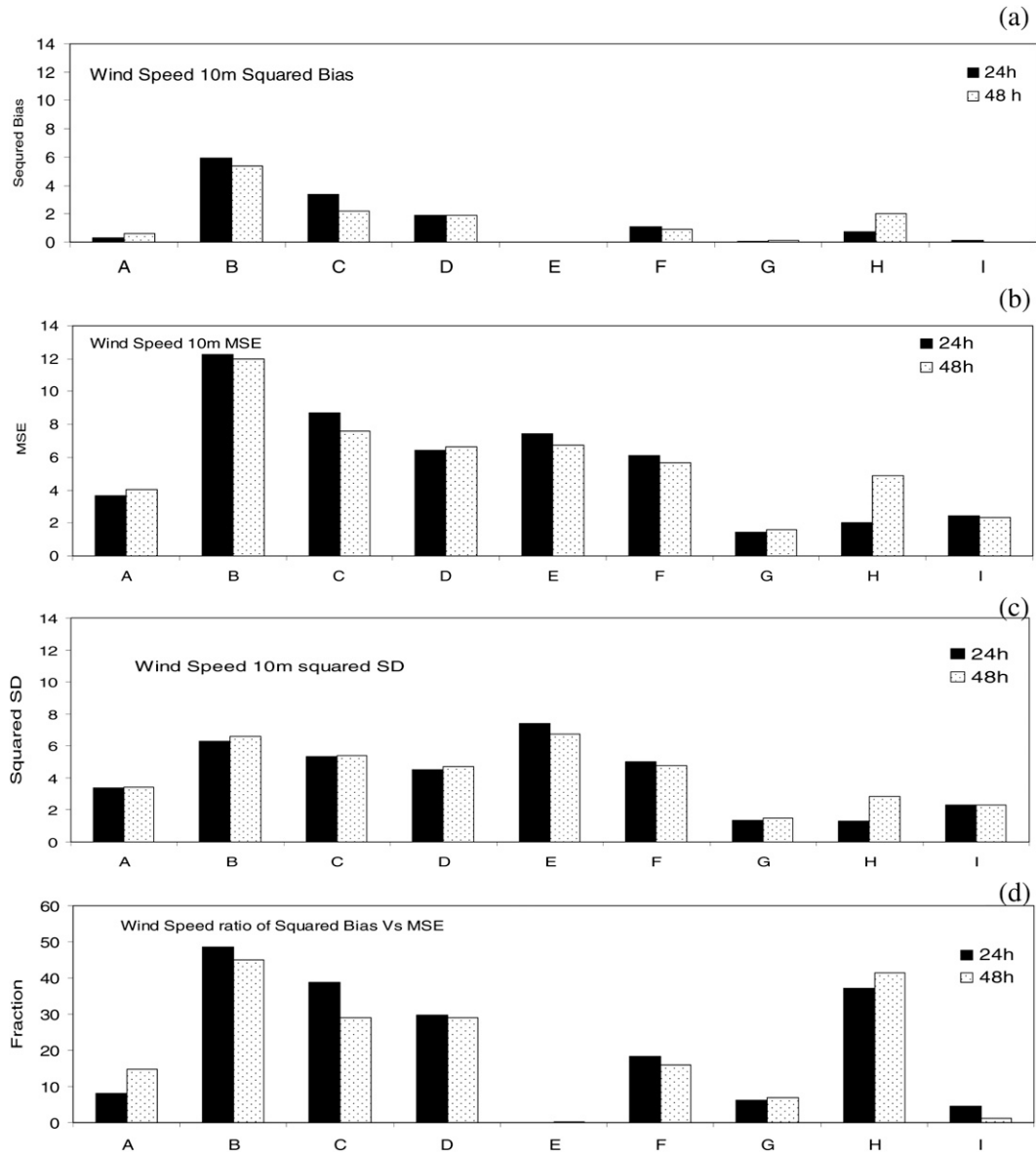


FIG. 6. Same as in Fig. 2 but for 10-m wind speed ( $m s^{-1}$ ) and 24-h forecasts only. Units are  $(m s^{-1})^2$  in (a)–(c).

low SD errors (Figs. 7b and 7c). The forecast errors from the systematic error in the western mountains of Iran are relatively large values (Fig. 7a). The 10-m wind speed statistical fields are quite different from the 2-m temperature fields, and the nonsystematic model errors compose a much larger portion of the total forecast errors for 2-m temperature forecasts (Fig. 7d). The 48-h forecast errors are similar to the 24-h forecast errors in most of the areas (not shown).

The above results suggest that the MSEs near the surface contain a substantial spatial heterogeneity, as can be seen by the relatively larger errors in the higher mountainous areas. However, the source of the errors indicates a significant

difference among the temperature, precipitation, and wind speed. The inaccuracies in the 2-m temperature forecasts come mainly from systematic errors, which are controlled largely by the physical representation within the model. In contrast, the inaccuracies in the precipitation and 10-m wind speed forecasts are dominated more by nonsystematic errors, which we postulate are derived from the random inadequacies of the initial conditions.

#### 4) TEMPERATURE AT 500 HPA

The squared bias is very small except that the Himalayan Mountains region (E) gets up to  $17^{\circ}C$  for 24-h forecasts (Fig. 8a) and there is a slightly larger value for

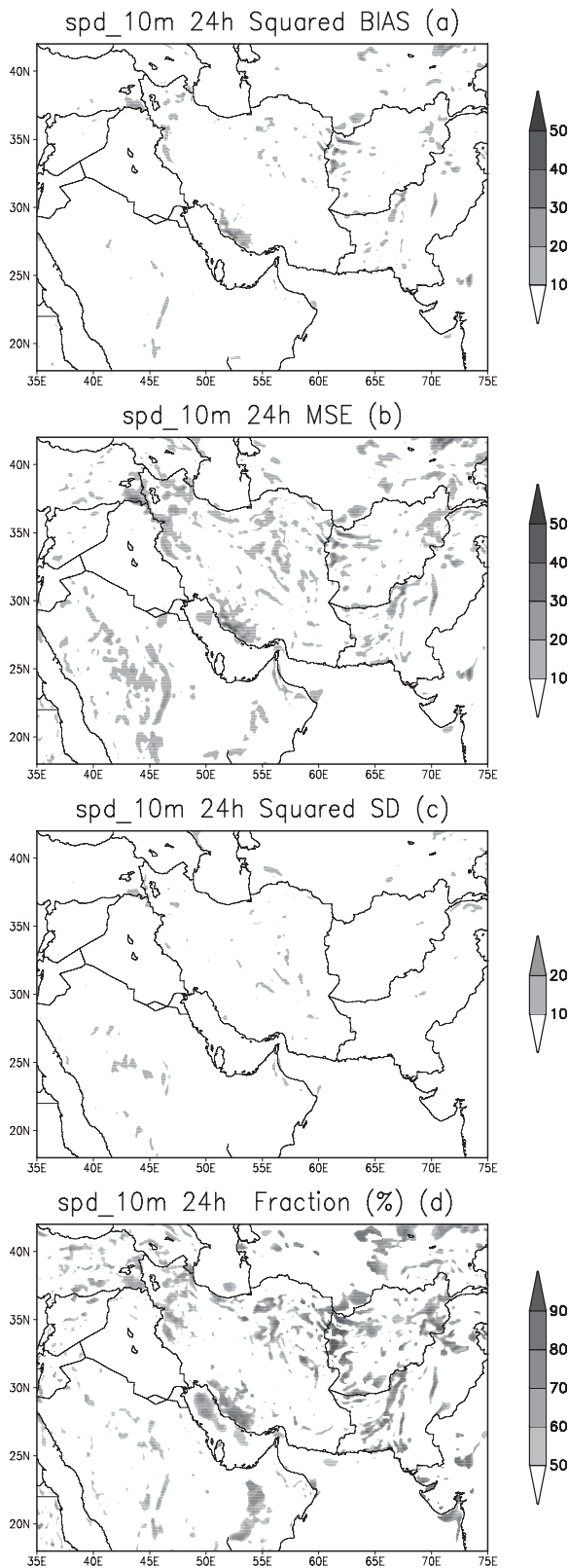


FIG. 7. Same as Fig. 3 but for 10-m wind speed and 24-h forecasts only. Units are  $(m s^{-1})^2$  in (a)–(c).

48-h forecasts (not shown). The larger magnitudes of the MSEs is randomly distributed over central Saudi Arabia, southeastern Iraq, northwestern Iran, and the western Himalayan Mountains (Fig. 8b). The corresponding SD error (Fig. 8c) reveals that nonsystematic errors compose a substantial portion of the total error. The fraction of squared biases to the MSE (Fig. 8d) is far less than 50% except for the western Himalayan Mountains region (E), which showed clearly that a larger contribution to the MSEs comes from a nonsystematic total model forecast error. Compared to 24-h forecasts, the 48-h forecasts' bias is higher over most of study areas (not shown).

5) WINDS AT 200 HPA

Similar to the upper-level temperature forecasts, the wind forecasts (the first 24-h forecasts shown only) at 200 hPa (Fig. 9) indicate that the MSEs are dominated by nonsystematic errors in either the zonal or meridional wind component or both. For the zonal wind forecasts, the large MSE over Himalayan Mountains region is consistent with nonsystematic error; in addition, the Arabian Sea also has a strong nonsystematic error signature. For the meridional wind component, the larger forecast errors occur over a different place from the zonal wind forecasts. The larger MSEs for the zonal wind forecasts in the Himalayan Mountains region disappear in the meridional wind field.

To summarize, the 2-m temperature forecast error is typically caused by systematic error and is most closely associated with the elevated terrain; by contrast, precipitation, 10-m wind speed, and upper level forecast errors are dominated by the nonsystematic errors, which do not appear to be correlated with terrain.

b. Diurnal cycle variation

Based on model forecasts, the southwest Asian domain-wide mean of the 2-m temperature exhibits a minimum near 0000 UTC followed by a sharp increase to a maximum near 1200 UTC (not shown). The differences in the variables (temperature, and wind speed) at maximum (1200 UTC) and minimum (0000 UTC) times are defined as the diurnal cycle variation in this study.

The southwest Asia area's mean diurnal cycle of 2-m temperature over the 30-day study period (Fig. 10a) shows that the amplitude of the temperature diurnal cycle for model forecasts is considerably lower than the value in the WMO GTS observations. Note a slight decrease in temperature diurnal cycle on 2, 7, and 17 January in GTS observations that is not observed in the model forecasts. These two points indicate that the near-surface temperature diurnal cycle in the model forecasts has serious problems.

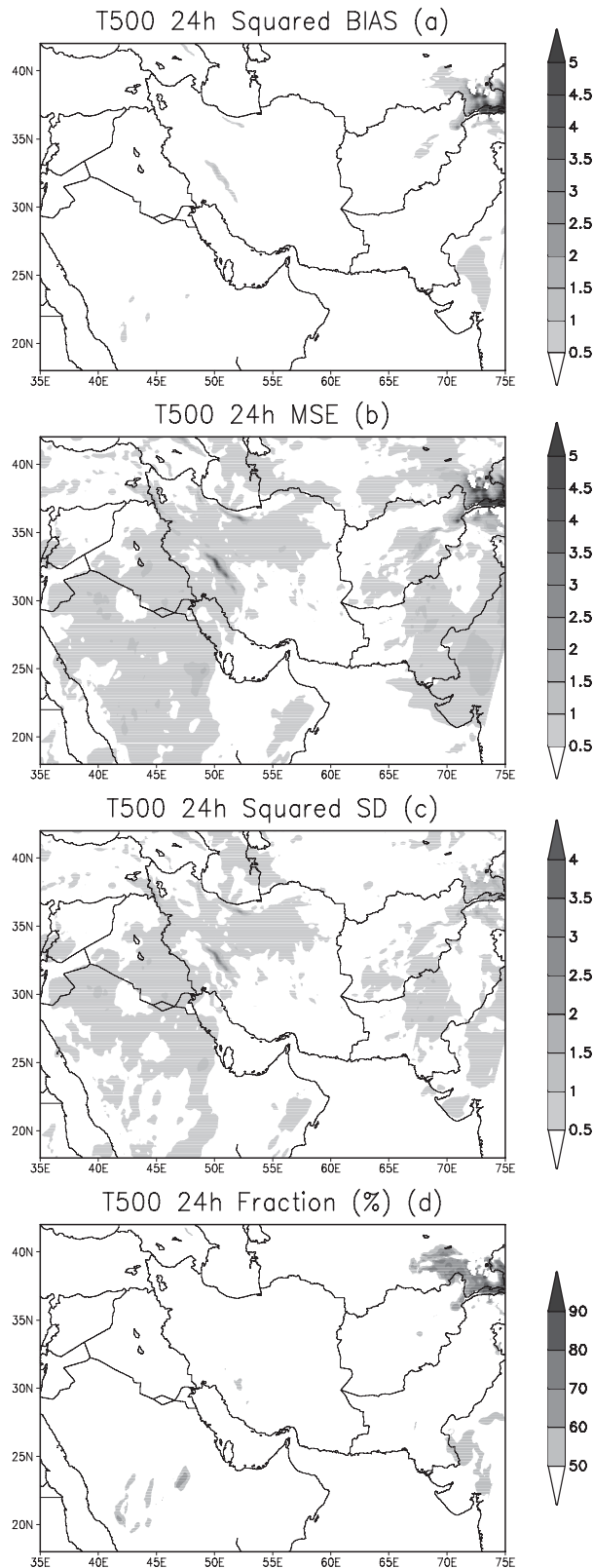


FIG. 8. Same as in Fig. 3 but for 500-hPa temperature and 24-h forecasts only. Unit is  $(^{\circ}\text{C})^2$  in (a)–(c).

The 10-m model forecast wind speeds exhibit a different pattern of behavior from that of temperature. Similar to the NCEP GFS analysis data, the amplitude of the wind speed diurnal cycle in the model (Fig. 10b) shows a strong daily variability. The magnitudes of the model forecasts values are fairly consistent with the analysis values, except for the large difference on 3 January. There is no evidence of a sharp gap between the model forecasts and the analysis data.

However, the spatial domain of the SWA areas appears to cover roughly four time zones. The whole domain average did not reflect significantly the diurnal cycle of the different locations. The 30-day period mean of the diurnal cycle (Fig. 11) displayed the variations among the locations. The results show that over regions in the western and northeastern parts of southwest Asia, including the Saudi Arabian desert and the northern border of Afghanistan, the model forecasts of 2-m temperature (Fig. 11b) are in much better agreement with the GTS observations (Fig. 11a) than in the Zagros Mountains of western Iran or in the northwest Indian deserts. Note that the amplitude of the diurnal cycle in the model is much smaller than the GTS observations.

For the diurnal cycle variation in 10-m wind speed, the model forecasts (Fig. 11d) over southwest Asia have similar amplitudes and distributions to the NCEP GFS analysis data (Fig. 11c) except for the clear mesoscale features in the model forecasts. Note, however, that the analysis data suggest a strong diurnal cycle variation over northwestern Iran and northern Afghanistan. Overall, however, the model forecasts of the diurnal cycle are consistent with the analysis.

## 6. Impact of satellite data assimilation

Results from the previous section suggest that, aside from the 2-m temperature, errors in most forecast variables are dominated by nonsystematic errors, which are caused by uncertainties in the model initial conditions or unresolvable differences in scales between the forecasts and the observations (Nutter and Manobianco 1999). The model initial conditions are very important factors impacting model forecasts. Many previous studies (Tracton et al. 1980; Halem et al. 1982; Andersson et al. 1991; Mo et al. 1995; Derber and Wu 1998; Bouttier and Kelly 2001) indicate that the assimilation of satellite radiance observations into a weather model can improve the forecasts by providing those initial conditions that are more representative of the true state of the atmosphere. For the purpose of understanding the role of initial conditions in the accuracy of forecasts, we will now consider satellite observation data assimilation.

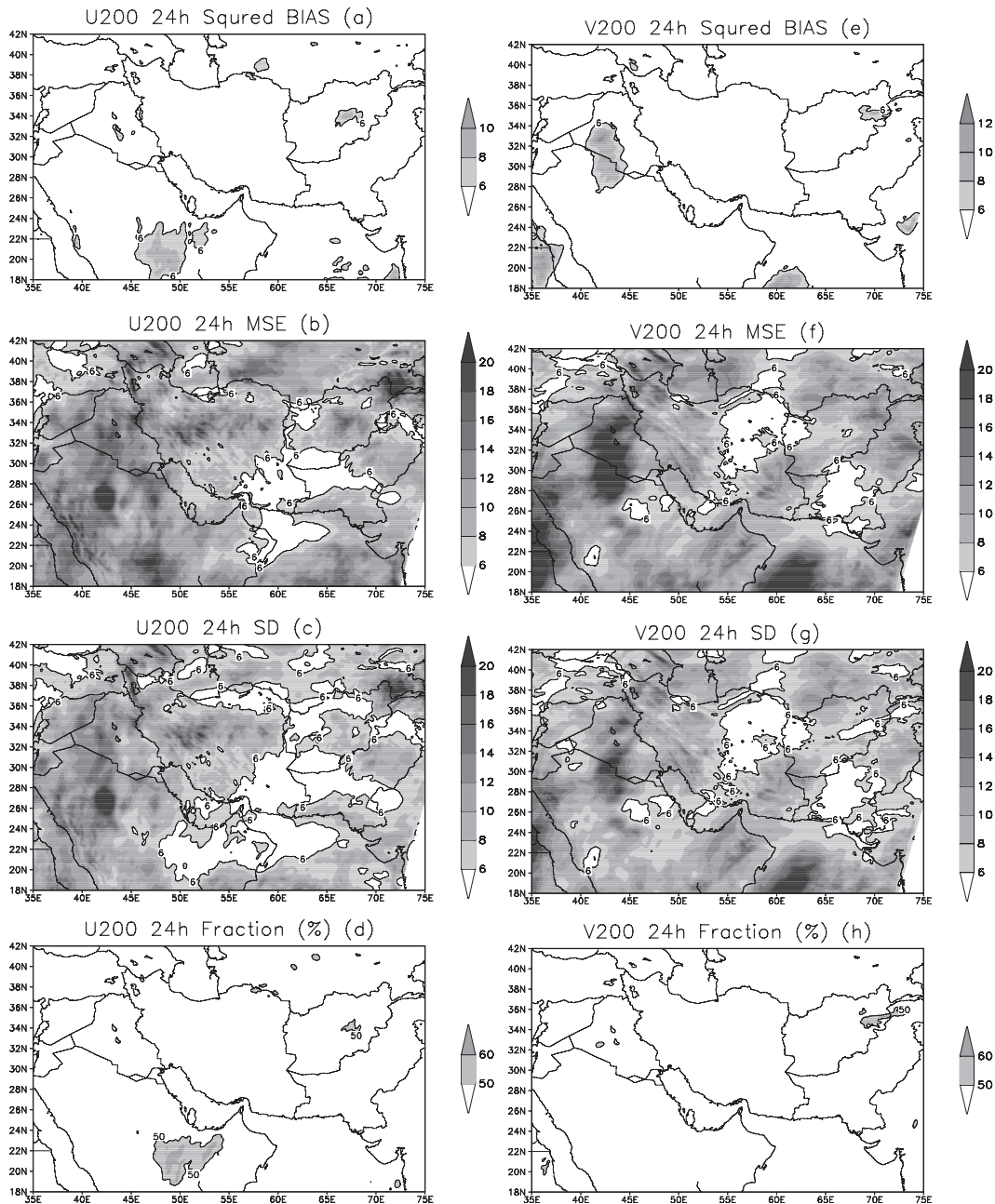


FIG. 9. Same as in Fig. 3 but for (a)–(d) 200-hPa zonal wind and (e)–(h) meridional wind for 24-h forecasts only.

### a. Data assimilation system

There are two basic approaches to assimilating satellite information into a data assimilation system (DAS). The first is to assimilate retrieved data from radiances measured by satellite instruments. The second is to assimilate radiance measurements directly into a DAS prior to the retrieval. Direct radiance assimilation is theoretically superior to retrieval assimilation because the observational error statistics in the former are more

justified than in the latter (Eyre et al. 1993; Derber and Wu 1998; McNally et al. 2000). Direct radiance assimilation will be used in the current study.

In this study, the Gridpoint Statistical Interpolation analysis system developed by JCSDA (Derber and Wu 1998; Cucurull et al. 2007) is integrated with the WRF-ARW mesoscale system, and the Advanced Television and Infrared Observation Satellite-N (TIROS-N) Operational Vertical Sounder (ATOVS) radiance observations are employed. The GSI analysis system is based

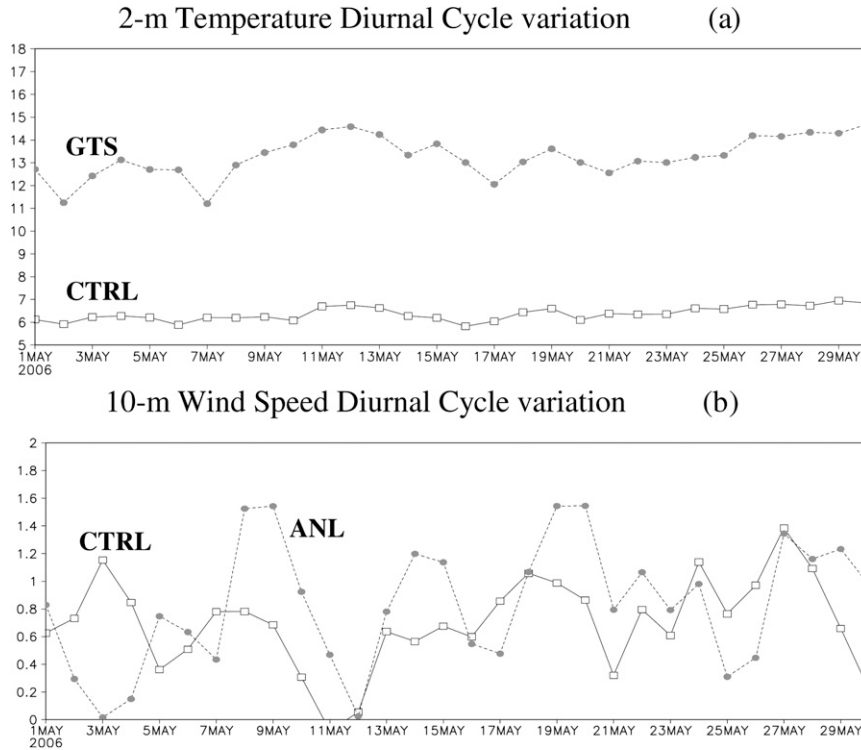


FIG. 10. Diurnal cycle variation of (a)  $T_{2m}$  ( $^{\circ}\text{C}$ ) and (b) 10-m wind speed ( $\text{m s}^{-1}$ ) for 24-h forecasts only.

on NCEP's three-dimensional variational data assimilation (3DVAR) analysis system known as Spectral Statistical Interpolation (SSI; Parrish and Derber 1992). The current GSI regional analysis system accepts NCEP's Nonhydrostatic Mesoscale Model (NMM) WRF and NCAR's ARW mass core (Liu and Weng 2006; Xu et al. 2009), and the input data could be either binary or network common data form (NetCDF) datasets. For the ARW regional model, the background error statistics in the GSI data assimilation system use the same vertical grid structure as the first-guess of NCEP global model forecasts. The background error covariance matrix is extracted through the interpolation of NCEP's GFS counterpart. The National Meteorological Center (NMC, now known as NCEP) method (Parrish and Derber 1992) is a popular method for estimating the climatological background error covariance.

#### b. Satellite data

The ATOVS datasets supplied by the National Environmental Satellite, Data, and Information Service (NESDIS) are composed of radiances from the Advanced Microwave Sounding Unit (AMSU) and the High-Resolution Infrared Sounder (HIRS/3). Two separate radiometers (AMSU-A and AMSU-B) compose the AMSU platform. AMSU-A is a cross-track, stepped-line

scanning total-power radiometer. The instrument has an instantaneous field of view of  $3.3^{\circ}$  at the half-power points, providing a nominal spatial resolution at nadir of 48 km. The AMSU-B is a cross-track, continuous-line scanning, total-power radiometer and has an instantaneous field of view of  $1.1^{\circ}$  (at the half-power points). The spatial resolution at nadir is nominally 16 km. The antenna provides a cross-track scan, scanning  $\pm 48.95^{\circ}$  from nadir with a total of 90 earth fields of view per scan line.

The AMSU-A and AMSU-B radiance data used here have undergone substantial preprocessing by NESDIS before becoming available. The data have been statistically limb corrected (adjusted to nadir) and surface emissivity corrected in the microwave channels. Figure 12 shows an example of the scan position of the two microwave sensors on board the *NOAA-15* and *-16* satellites during the study period. It is clear that the *NOAA-16* data cover the most southwest Asia area and AMSU-B has a higher density of observations than the AMSU-A.

Derber and Wu (1998) pointed out that the presence of a single data point containing large errors can result in substantial degradation of the analysis and the subsequent forecast. For this reason, a simple quality control procedure has been developed and the observed

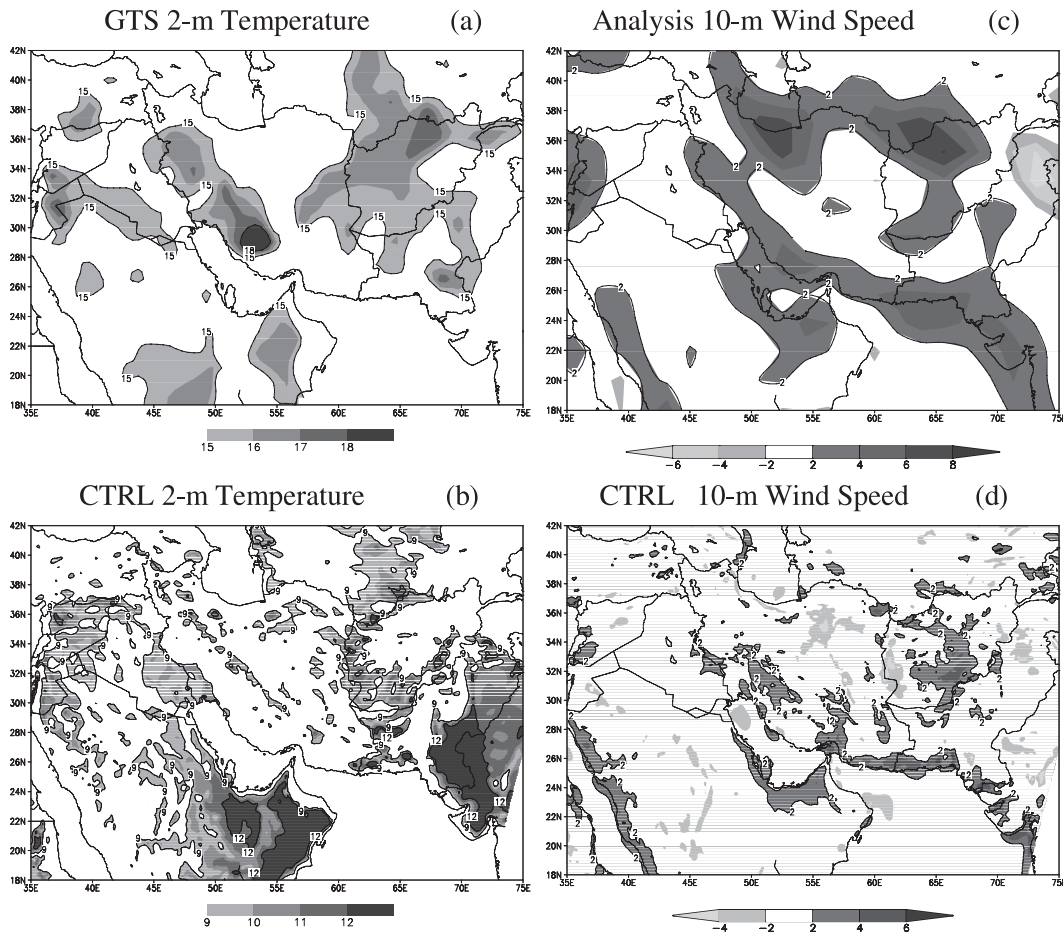


FIG. 11. Diurnal cycle variations of  $T_{2m}$  ( $^{\circ}\text{C}$ ) in (a) GTS observations, (b) CTRL model forecasts and 10-m wind speed ( $\text{m s}^{-1}$ ) in the (c) NCAR GFS analysis and (d) CTRL model forecasts for 24-h forecasts only.

brightness temperature data have been modified empirically with various parameters for different instruments. In the GSI analysis system, this check includes two steps. First, a location check (including removal of observations outside the domain) and a thinning procedure (excluding location-time duplicates and incomplete observations) are performed to ensure the vertical consistency of upper-air profiles. Second, numerous quality control (QC) checks are redone based on various quality parameters after the model brightness temperatures are obtained from the radiative transfer model. The quality parameters are formulated in terms of the expected observational error variance as a function of the channels and have been adjusted for their position across the track of the scan, whether it is over land, sea, snow, sea ice, or a transition region, and for elevation, the difference between the model and the real topography, and, finally, the latitude. In Fig. 13, the statistics show that the number of observations used in the GSI regional data assimilation system is quite different.

AMSU-B has many more observations than do the two AMSU-A platforms. For *NOAA-15* (Fig. 13), the maximum number of AMSU-B observations for all 30 days range from 50 000 to 150 000 pixels, and for AMSU-A, the number is only around 40 000 pixels. For *NOAA-16*, the number of AMSU-B observations exceeded 150 000 pixels, while the AMSU-A was under 60 000 pixels. On average for the 30 days, the evidence shows that through this two-step checking procedure, the amount of radiance data going into the model is substantially reduced. The percent usage of AMSU-A radiance data was over 40%, but for AMSU-B it was only 16%.

It is obvious that bias correction and quality control remove nonuseful data. This is less taxing on the minimization procedure within variational data assimilation systems. However, because of the imperfections inherent in the bias correction and quality control schemes, a lot of valuable observations are eliminated. Future studies should continue to refine the bias correction and quality control schemes.

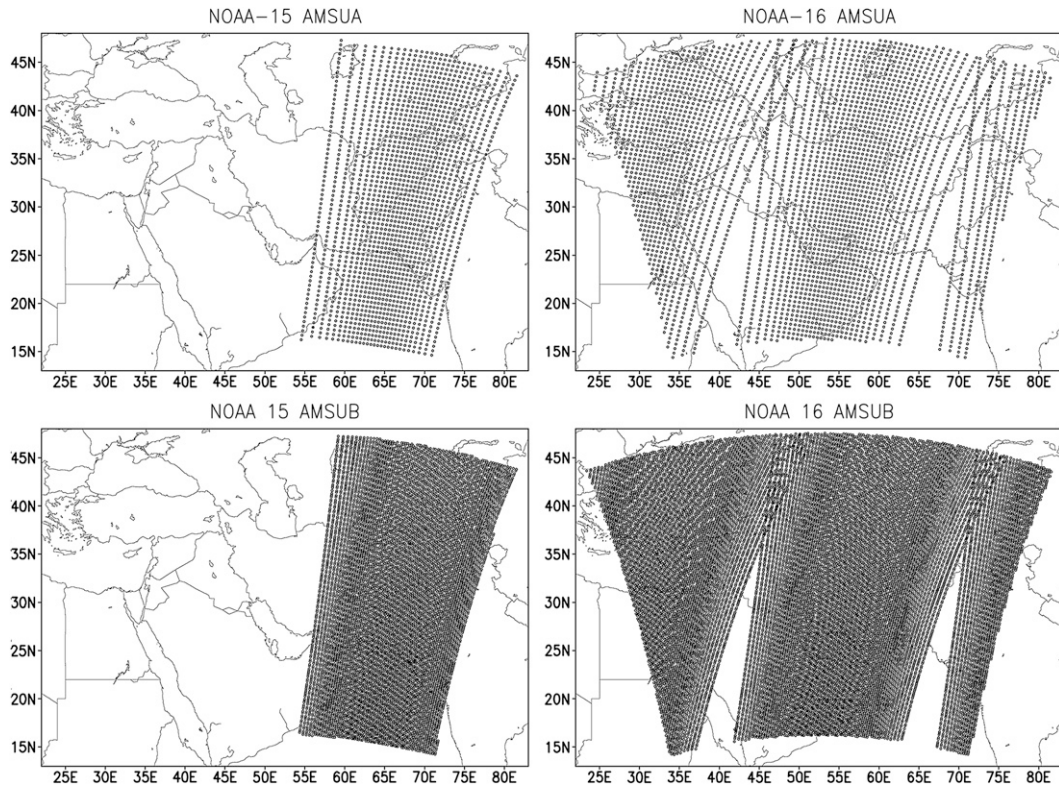


FIG. 12. Scan coverage of ATOVS (AMSU-A and -B) radiance being used in the current data assimilation system at 0000 UTC during May 2006.

### c. Experiments design

For the control experiments described in section 2 (referred to as CTRL), the initial conditions generated from the GFS forecasts had been assimilated with several satellite data sources, such as AMSU-A/B, HIRS, the Microwave Sounding Unit (MSU), etc. For the purpose of eliminating the effects of these radiance assimilations in the first-guess field from the GFS global analysis data, we first generated a spinup run for 6 h from 1800 UTC on the previous day to 0000 UTC on the forecasting day in the data assimilation (referred to as DA) experiments, then the AMSU-A and AMSU-B radiance data are assimilated in the ARW forecast model to modify the initial conditions at 0000 UTC on each day, and finally we produce forecasts in the same way as the CTRL experiment.

### d. Results analysis

To understand clearly the effects of the ATOVS radiance data assimilation on the forecasts over the study area, three statistical variables—bias, correlation, and mean square error skill score—are calculated against the observation data.

#### 1) BIAS

The bias is computed as in Eq. (1), and the absolute bias difference between DA and CTRL is defined as  $|\text{bias}|_{\text{DA}} - |\text{bias}|_{\text{CTRL}}$ . The 30-day mean will be investigated first. For the 24-h forecasts, the absolute bias difference in the 2-m temperature forecast (Fig. 14a) shows that the bias is reduced in DA over most of southwest Asia. The biases in Iran, Afghanistan, and Pakistan are on average 0.3°–1.8°C less than in the CTRL forecasts, with the largest impact occurring on the south or southwest slope of the Afghanistan Hindu Kush Mountains area (cf. with Fig. 1).

The absolute bias difference in 10-m wind speed for the 24-h forecasts (Fig. 14b) reveals that the largest impacts on DA are over the Arabian Sea, the Persian Gulf, and the border area between Pakistan and Afghanistan, where these places are beyond the effects of high terrain. Whereas the impact of the satellite data assimilation on the 2-m temperature is observed near the mountain areas, the impact on the 10-m wind speed happens in places far away from these mountain regions, and especially over water areas. However, the evidence shows that the bias increased in many areas including south-eastern Iran, northwestern India, and the other areas.

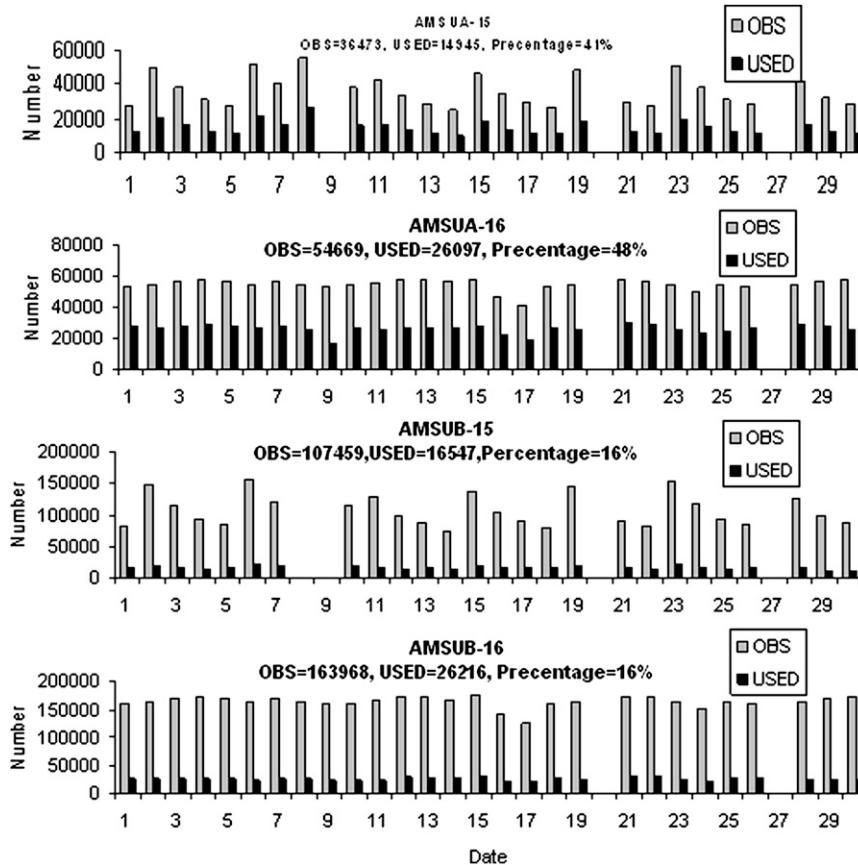


FIG. 13. Total amount of radiance and the used percentage in the forecast experiments as a function of date for AMSU-A and AMSU-B in NOAA-15 and NOAA-16, respectively.

Compared to the 24-h forecasts in the CTRL experiment, the precipitation forecast bias with DA (Fig. 14c) decreased slightly over the Mediterranean Sea, the Black Sea coast, the Saudi Arabian desert, and the Iranian Zagros Mountains areas. Note, however, the bias with DA increased over the Himalayan Mountains area.

For upper levels, the absolute bias difference in the 500-hPa temperature, geopotential height, and wind field forecasts are presented in Fig. 15. The radiance data assimilation reduces the forecast bias of the geopotential height (Fig. 15b) and wind field (Figs. 15c and 15d) over most of southwest Asia. The evidence shows that the upper-level geopotential height and wind field forecasts impacted by satellite radiance data assimilation are not associated with the configuration of terrain. Meanwhile, the 500-hPa temperature forecasts are modulated by the radiance assimilation differently (Fig. 15a). Here, the satellite data assimilation does not improve the temperature forecasts over the central southwest Asia area, including Saudi Arabia, the Iranian Zagros Mountains, and the Afghan Hindu Kush Mountains.

## 2) MEAN-SQUARE-ERROR SKILL SCORES

Murphy (1988) found forecasting skill scores are generally defined as measures of the relative accuracy of two forecasts, where one of the two forecasts is defined as a “reference system.” For the following experiments, the CTRL forecasts are considered to be the reference system. Based on the mean-square error, the skill score (SS) can be expressed as follows:

$$SS(d, r, a) = 1 - [MSE(d, a)/MSE(r, a)]. \quad (6)$$

Note that SS in Eq. (6) is a function of the DA forecasts ( $d$ ), the CTRL reference forecasts ( $r$ ), and the analyzed quantity ( $a$ ). The  $MSE(d, a)$  and  $MSE(r, a)$  are as defined in Eq. (2) indicating the mean-square error of DA and the CTRL forecast relative to the analysis, respectively. Therefore, the greater positive SS values reflect increasing positive skill over the performance of the reference forecasts.

Figure 16 depicts the results for the 2-m temperature, 10-m wind speed, and precipitation forecasts over the nine locations defined in Fig. 1. With regard to the 2-m

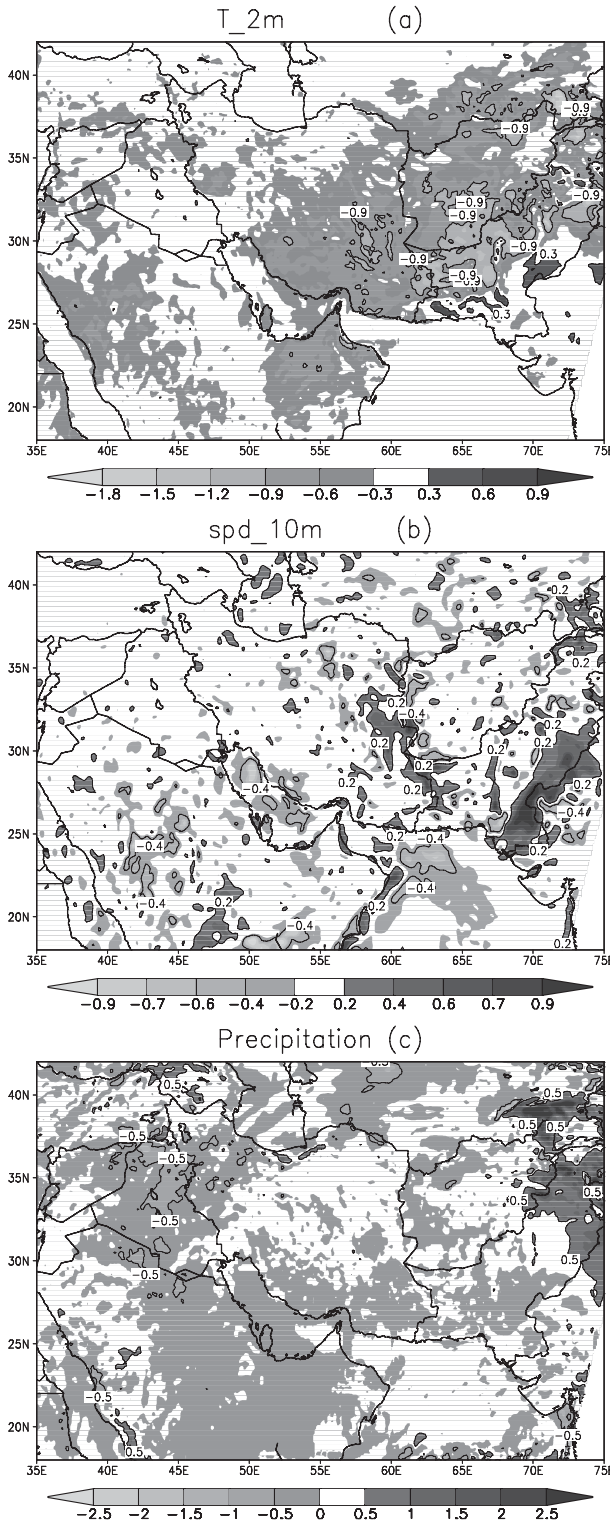


FIG. 14. Bias (model – observation) of (a)  $T_{2m}$  ( $^{\circ}C$ ), (b) 10-m wind speed ( $m s^{-1}$ ), and (c) precipitation ( $mm day^{-1}$ ) for 30-day-averaged 24-h forecasts during May 2006.

temperature forecasts, the statistical analysis (Fig. 16a) indicates that all SSs in the different locations are positive for the 24- and 48-h forecasts, but the SSs for 48-h forecasts in most regions are greatly diminished in relation to those of the 24-h forecasts. The SSs in the northern Iranian Zagros Mountains (B) and the western Himalayan Mountains (E) are about 10%–20% less than those in the lower mountains or plain areas. When compared to Fig. 2, we find that the forecast errors in the high-mountain areas are mainly from the model systematic errors and the nonsystematic errors make a relatively smaller contribution to the total forecast error. Satellite data assimilation, at least for the AMSU-A and AMSU-B radiances, seems not to make a significant contribution to the accuracy of the surface temperature forecasts in the higher-mountain areas.

In contrast, the 10-m wind speed in Fig. 16b shows a inverse SS value from the surface temperature. Six of nine locations including all high-mountain areas (B, D, and E) show a negative skill score, which means the satellite data assimilation produced a negative impact, but the SSs in the Arabian Sea increase by 25% and 20% for 24- and 48-h forecasts, respectively. For the precipitation forecasts, the evidence shows (Fig. 16c) that the satellite data assimilation only improved the model forecasting bias over Iraq (A), northern Iran (B), and the Saudi Arabia desert (F, G). The other five subregions became worse.

### 3) PATTERN CORRELATION

To evaluate the spatial agreement between the model and the observations quantitatively, pattern correlations (Walsh and McGregor 1997) were calculated between the model-simulated and observed fields. The pattern correlation  $\rho_p$  of the two spatial fields is simply the correlation of a series of points ( $i$ ) from one field with corresponding values from the other field:

$$\rho_p = \frac{\sum(X_{oi} - \bar{X}_o)(X_{fi} - \bar{X}_f)}{\sqrt{\sum(X_{oi} - \bar{X}_o)^2} \sqrt{\sum(X_{fi} - \bar{X}_f)^2}}, \quad (7)$$

where  $\bar{X}_o$  and  $\bar{X}_f$  are the means of the observational field ( $X_o$ ) and model-simulated field ( $X_f$ ), respectively.

Figure 17 shows the pattern correlation of the observational and model forecasting fields for 2-m temperature, 10-m wind speed, and precipitation over the whole prediction domain. The pattern correlation coefficient between the observations and model forecasts grows slightly after satellite data assimilation for these three surface variables in each of the 24- and 48-h forecasts. For a 30-day average in 24-h forecasts (Figs. 17a–c),

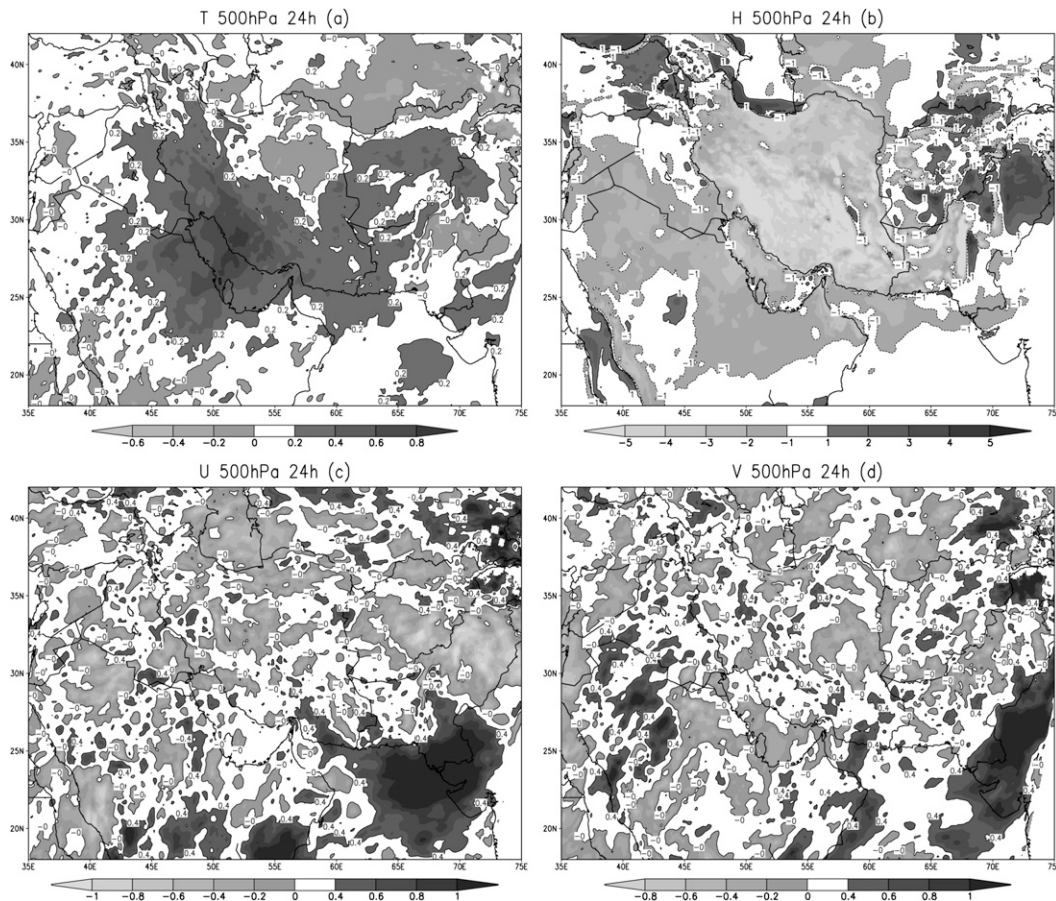


FIG. 15. Bias (model – observation) of (a) temperature ( $^{\circ}\text{C}$ ), (b) geopotential height (gpm), (c) zonal wind ( $\text{m s}^{-1}$ ), and (d) meridional wind ( $\text{m s}^{-1}$ ) at 500 hPa for 30-day-averaged 24-h forecasts during May 2006.

the correlation coefficient in the CTRL reaches 0.973, 0.268, and 0.575 for 2-m temperature, 10-m wind speed, and precipitation, respectively. The corresponding values in DA are 0.975, 0.280, and 0.581. The 48-h forecasts have similar results (Figs. 17d–f). The results indicate that the pattern forecasts' improvement is very limited although the correlation coefficient grows in DA.

#### 4) NEAR-SURFACE TEMPERATURE AND WIND FIELD DIURNAL CYCLE VARIABILITY

Analysis of near-surface temperature and wind field variability is based on eight selected subregions [the Arabian Sea (H) was omitted due to there being no GTS temperature data available there]. The 30-day mean diurnal cycle variation of 2-m temperature is presented in Fig. 18. It is apparent that the amplitudes of the diurnal cycles in the model forecasts of temperature in the CTRL and DA are relatively lower than in the GTS observations over seven of eight selected subregions (Fig. 18a). Note that the amplitude of the diurnal cycle in DA is closer to the GTS observations although

the growth is very small. This demonstrates that the surface air temperature diurnal cycle can be improved slightly with satellite data assimilation.

For analysis of the 10-m wind fields, the reference data used are still those of the NCEP GFS analysis. In contrast to surface temperature, it is not readily apparent that the amplitude of the diurnal cycle has been improved in DA (Fig. 18b). The performances are quite different in these selected subregions. The diurnal cycle of the wind speed (Fig. 18b) in the analysis data is considerably larger than in the model forecasts over the five subregions B, D, E, H, and I, where B, D, and E are three high-mountain subregions. But it is clear that the amplitude of the diurnal cycle has been modified to some degree in DA.

## 7. Summary and discussion

### a. Summary

This paper presented an objective verification and impact of radiance data assimilation on weather forecasts

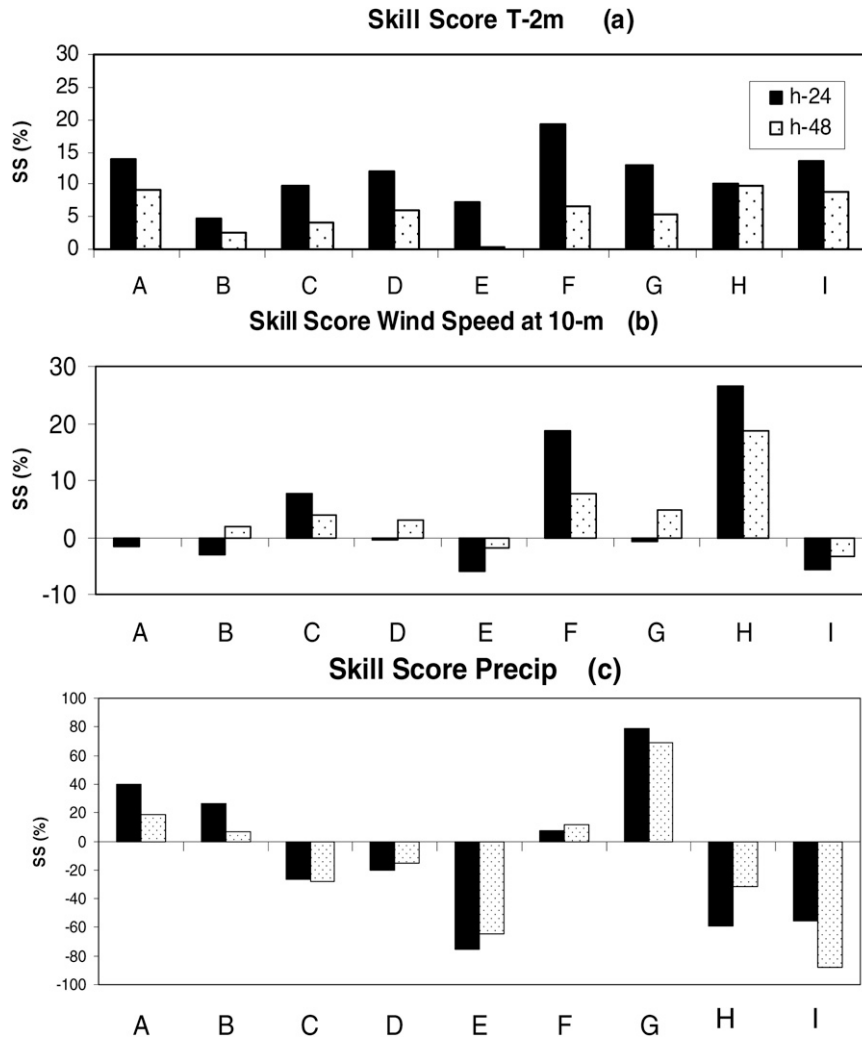


FIG. 16. MSE SSs for (a)  $T_{2m}$ , (b) 10-m wind speed, and (c) 24-h accumulated precipitation. Results are plotted for averaged 24- and 48-h forecasts as a function of defined locations.

over complex terrain areas of southwest Asia using the NCAR mesoscale model (WRF-ARW) and the Joint Center for Satellite Data Assimilation (JCSDA) analysis system (GSI). The experiment period was from 1 through 31 May 2006. The results are summarized as follows.

The model biases caused by inadequate parameterization of physical processes, except for the 2-m temperature, are relatively small compared to the nonsystematic errors resulting, in part, from the uncertainty in the initial conditions. The total forecast errors at the surface show a substantial spatial heterogeneity; there is relative larger error in higher-mountain areas. However, the source of the error indicates a unique difference between the temperature, precipitation, and wind speed, where the error in 2-m temperature is mainly from systematic errors, which are largely controlled by

the physical representation of the terrain (i.e., the errors are positively correlated with terrain elevation); while, in contrast, the errors in 10-m wind speed and precipitation have a greater contribution from nonsystematic errors, which are more likely related to uncertainty in the initial conditions.

The amplitude of the diurnal cycle of 2-m temperature in the model is much smaller than the GTS observations. However, the model forecasts of the diurnal cycle are consistent with the NCEP GFS analysis data. There is no evidence of a noticeable gap between the model forecasts and the analysis data.

The ATOVS satellite data provides useful information for improving the initial conditions, and the model error was reduced to some degree. The bias and mean-square error skills score (SS) show that satellite data assimilation produces a better forecast over some of areas; however, it

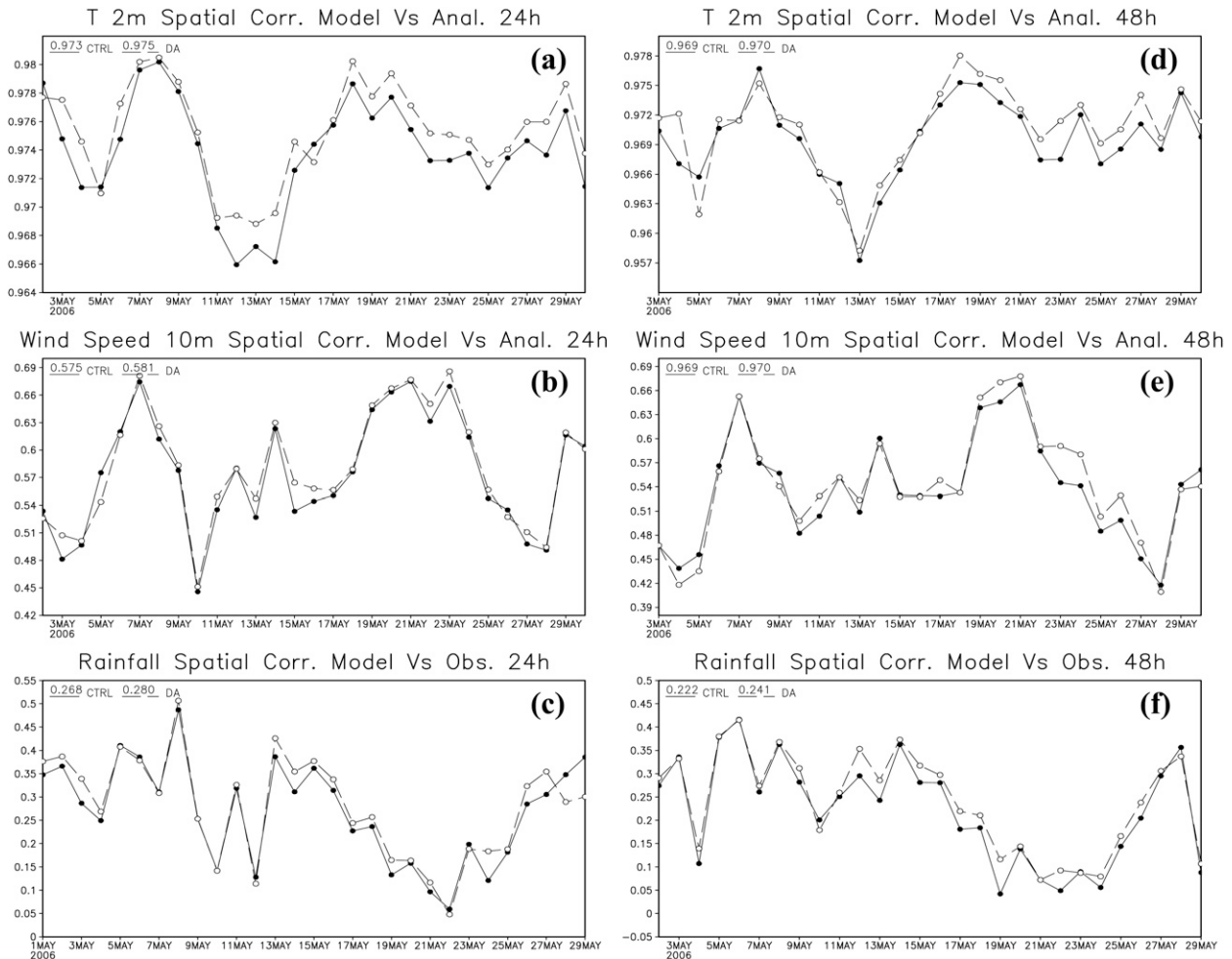


FIG. 17. Pattern correlation of model forecasts and observation of  $T_{2m}$ , 10-m wind speed, and rainfall for (a)–(c) 24- and (d)–(f) 48-h forecasts.

does not seem to make a significant contribution to the accuracy of forecasts in the higher-mountain areas. The pattern forecasts show improvement in DA, although its correlation coefficient growth is very small.

### b. Discussion

In this study, the weather forecasts using the WRF-ARW system were evaluated over the mountainous areas of southwest Asia. Due to the complexity of the high terrain and lack of knowledge in the estimation of the physical processes in this area, forecasters should have greater awareness of these limitations of the model when forecasting in this region.

First of all, parameterization of physical processes plays a significant role in the forecasting of surface temperature. For the 2-m temperature forecasts, the systematic error component is not only larger than the random errors, but also indicates it is related to the el-

evaluation of the terrain. Meanwhile, we note that the areas of high bias shown in Fig. 3a correspond more with areas of rapid elevation change. These are the areas where a difference in terrain height between the datasets would have the largest effect. They are also the areas where differences between the observational station elevation and the mean grid-point elevation would be largest. The lapse rate effects due to these terrain height differences are probably another reason for the 2-m temperature bias. In contrast, random errors play a much bigger role in the forecasting of the upper-level, precipitation, and 10-m wind fields. The random errors prevent perfect forecast guidance and are caused by a combination of the uncertainty in the initial conditions and unreasonable model scales. The detailed statistical results presented in section 4 are specific to the surface and the upper level at nine specific locations. The basic error characteristics for one forecasting variable vary by the selected locations,

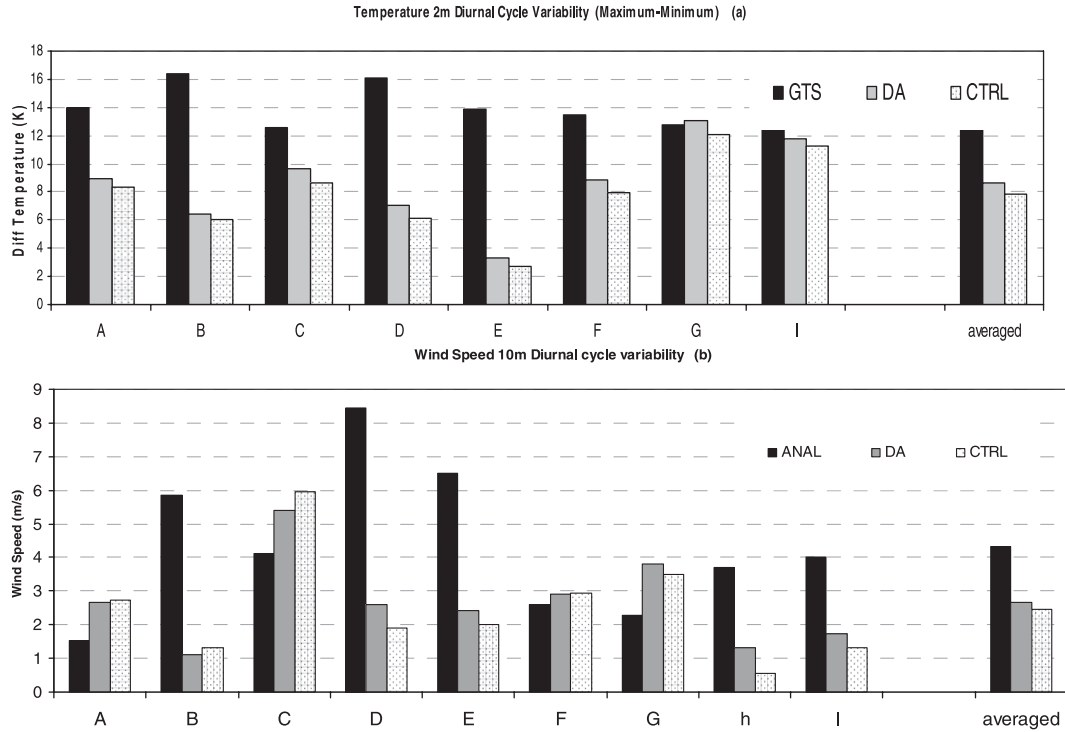


FIG. 18. Diurnal cycle variations over the defined location for (a)  $T_{2m}$  ( $^{\circ}\text{C}$ ) and (b) 10-m wind speed ( $\text{m s}^{-1}$ ).

and may not be representative of errors of other forecast variables. For example, in a preliminary investigation of temperature errors, the results demonstrated that the maximum 2-m temperature biases occurred over the high-mountain areas while the temperature biases at 500 hPa were found over most of southwest Asia and were not related to the configuration of the terrain.

Note that the results presented here are for only 1 month of experimental model runs; the accuracy of the forecasts' performance needs to be further verified and investigated with more real-time forecasts. As expressed by Manning and Davis (1997), "These statistics would provide additional information to model users and alert model developers to those research areas that need more attention." The additional and complementary need for verification strategies in the WRF-ARW model is elucidated in reference papers (e.g., Skamarock et al. 2005).

Second, random error is very complicated. It is only partially attributable to the uncertainty in the initial conditions. An accurate representation of the initial conditions would help users to compare the latest forecast guidance with the current observations and make appropriate adjustments in real time. The assimilation of satellite radiance observations into a numerical weather prediction (NWP) model provides initial conditions more closely representative of the true state

of the atmosphere. The results shown here demonstrate the positive impacts of satellite data on weather prediction in most of the southwest Asia areas, but the impacts are not as obvious in the high-terrain areas, such as the Himalayan Mountains and the Iranian mountain region. This feature implies that the random error is not only derived from the uncertainty in the initial conditions, but that there are other reasons, like the resolution of the model horizontal scale, that also needs to be considered. This issue will be investigated in future work.

*Acknowledgments.* The authors thank Dr. Russ Treadon from JCSDA for answering many questions regarding the WRF-ARW and the GSI data assimilation system. The suggestion by one of the reviewers, Dr. Evans, to examine the lapse rate effects strengthened the conclusions. We also thank two other anonymous reviewers for their valuable comments and suggestions.

REFERENCES

Agrawala, S., M. Barlow, H. Cullen, and B. Lyon, 2001: The drought and humanitarian crisis in central and southwest Asia: A climate perspective. IRI Special Rep. 01-11, International Research Institute for Climate Prediction, Lamont-Doherty Earth Observatory, Columbia University, Palisades, NY, 20 pp. [Available from Lamont-Doherty Earth Observatory, Columbia University, Palisades, NY 10964.]

- Andersson, E., A. Hollingsworth, G. Kelly, P. Lönnberg, J. Pailleux, and Z. Zhang, 1991: Global observing system experiments on operational statistical retrievals of satellite sounding data. *Mon. Wea. Rev.*, **119**, 1851–1864.
- Bouttier, F., and G. Kelly, 2001: Observing-system experiments in the ECMWF 4D-Var data assimilation system. *Quart. J. Roy. Meteor. Soc.*, **127**, 1469–1488.
- Cheng, Y. Y., and W. J. Steenburgh, 2005: Evaluation of surface sensible weather forecasts by the WRF and the Eta Models over the western United States. *Wea. Forecasting*, **20**, 812–821.
- Cucurull, L., J. C. Derber, R. Treadon, and R. J. Purser, 2007: Assimilation of global positioning system radio occultation observations into NCEP's Global Data Assimilation System. *Mon. Wea. Rev.*, **135**, 3174–3193.
- Derber, J. C., and W.-S. Wu, 1998: The use of TOVS cloud-cleared radiances in the NCEP SSI analysis system. *Mon. Wea. Rev.*, **126**, 2287–2299.
- Evans, J. P., and R. Smith, 2001: Modelling the climate of south west Asia. *Proc. Int. Congress on Modelling and Simulation (MODSIM01)*, Canberra, ACT, Australia, Modelling and Simulation Society of Australia and New Zealand Inc. [Available online at <http://www.mssanz.org.au/MODSIM01/Vol%202/Evans.pdf>.]
- , and —, 2006: Water vapor transport and the production of precipitation in the eastern Fertile Crescent. *J. Hydrometeorol.*, **7**, 1295–1307.
- , —, and R. J. Oglesby, 2004: Middle East climate simulation and dominant precipitation processes. *Int. J. Climatol.*, **24**, 1671–1694.
- Eyre, J. R., G. Kelly, A. P. McNally, E. Andersson, and A. Persson, 1993: Assimilation of TOVS radiances through one dimensional variational analysis. *Quart. J. Roy. Meteor. Soc.*, **119**, 1427–1463.
- Gallus, W. A., Jr., and J. F. Bresch, 2006: Comparison of impacts of WRF dynamic core, physics package, and initial conditions on warm season rainfall forecasts. *Mon. Wea. Rev.*, **134**, 2632–2641.
- Halem, M., E. Kalnay, W. E. Baker, and R. Atlas, 1982: An assessment of the FGGE satellite observing system during SOP-1. *Bull. Amer. Meteor. Soc.*, **63**, 407–429.
- Liu, Q., and F. Weng, 2006: Detecting the warm core of a hurricane from the Special Sensor Microwave Imager Sounder. *Geophys. Res. Lett.*, **33**, L06817, doi:10.1029/2005GL025246.
- Lorenz, E. N., 1963: The mechanics of vacillation. *J. Atmos. Sci.*, **20**, 448–465.
- Manning, K. W., and C. A. Davis, 1997: Verification and sensitivity experiments for the WISP95 MM5 forecasts. *Wea. Forecasting*, **12**, 719–735.
- Marcella, M. P., and E. A. Eltahir, 2008: Modeling the hydroclimatology of Kuwait: The role of subcloud evaporation in semiarid climates. *J. Climate*, **21**, 2976–2989.
- McNally, A. P., J. C. Derber, W. Wu, and B. B. Katz, 2000: The use of TOVS level-1b radiances in the NCEP SSI analysis system. *Quart. J. Roy. Meteor. Soc.*, **126**, 689–724.
- Michalakes, J., S. Chen, J. Dudhia, L. Hart, J. Klemp, J. Middlecoff, and W. Skamarock, 2001: Development of a next generation regional weather research and forecast model. *Developments in Teracomputing: Proceedings of the Ninth ECMWF Workshop on the Use of High Performance Computing in Meteorology*, W. Zwiefelhofer and N. Kreitz, Eds., World Scientific, 269–276.
- Mo, K. C., X. L. Wang, R. Kistler, M. Kanamitsu, and E. Kalnay, 1995: Impact of satellite data on the CDAS–reanalysis system. *Mon. Wea. Rev.*, **123**, 124–139.
- Murphy, A. H., 1988: Skill scores based on the mean square error and their relationships to the correlation coefficient. *Mon. Wea. Rev.*, **116**, 2417–2424.
- Nutter, P. A., and J. Manobianco, 1999: Evaluation of the 29-km Eta Model. Part I: Objective verification at three selected stations. *Wea. Forecasting*, **14**, 5–17.
- Parrish, D. F., and J. C. Derber, 1992: The National Meteorological Center's Spectral Statistical Interpolation Analysis System. *Mon. Wea. Rev.*, **120**, 1747–1763.
- Skamarock, W. C., J. B. Klemp, J. Dudhia, D. O. Gill, D. M. Barker, W. Wang, and J. G. Powers, 2005: A description of the Advanced Research WRF. Version 2. NCAR Tech. Note NCAR/TN-468+STR, 94 pp.
- Tracton, M. S., A. J. Desmarais, R. J. van Haaren, and R. D. McPherson, 1980: The impact of satellite soundings on the National Meteorological Center's analysis and forecast system—The Data Systems Test results. *Mon. Wea. Rev.*, **108**, 543–586.
- Walsh, K., and J. McGregor, 1997: An assessment of simulations of climate variability over Australia with a limited area model. *Int. J. Climatol.*, **17**, 201–223.
- Xie, P., and P. A. Arkin, 1996a: Analysis of global monthly precipitation using gauge observations, satellite estimates, and numerical model prediction. *J. Climate*, **9**, 840–858.
- , B. Rudolf, U. Schneider, and P. Arkin, 1996b: Gauge-based monthly analysis of global land precipitation from 1971 to 1994. *J. Geophys. Res.*, **101** (D14), 19 023–19 034.
- Xu, J., S. Rugg, M. Horner, and L. Byerle, 2009: Application of ATOVS radiance with ARW WRF/GSI data assimilation system in the prediction of Hurricane Katrina. *Open Atmos. Sci. J.*, **3**, 13–28.
- Zaitchik, B. F., J. P. Evans, R. A. Geerken, and R. B. Smith, 2007a: Climate and vegetation in the Middle East: Interannual variability and drought feedbacks. *J. Climate*, **20**, 3924–3941.
- , —, and R. B. Smith, 2007b: Regional impact of an elevated heat source: The Zagros plateau of Iran. *J. Climate*, **20**, 4133–4146.